Mathematical Problems in Engineering

Intelligent Monitoring, Diagnosis and Prognosis for Electromechanical Equipment

Lead Guest Editor: Zhi-Xin Yang
Guest Editors: Li-Jun Zhou, Xian-Bo Wang, and Om Prakash Yadav

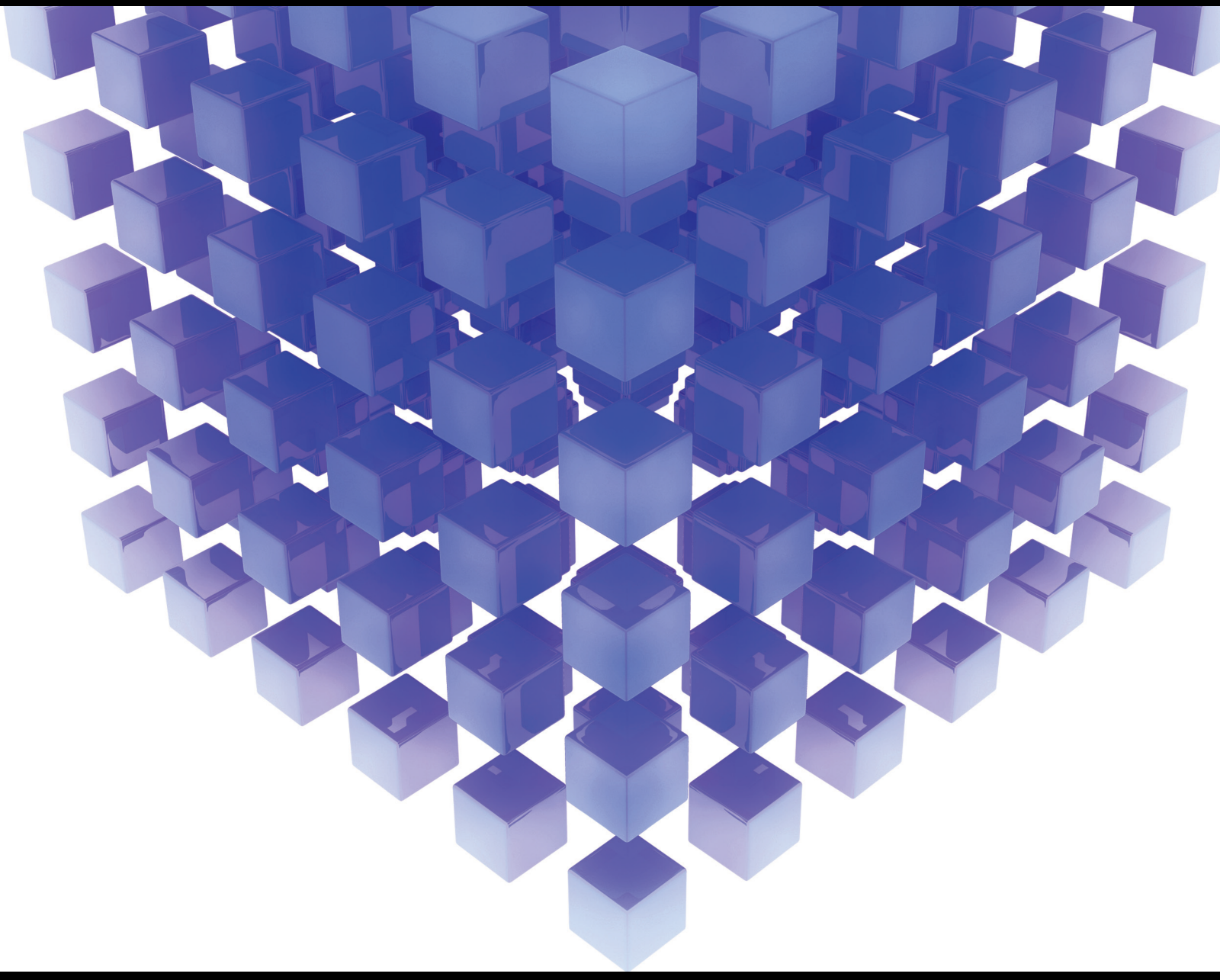

Intelligent Monitoring, Diagnosis and Prognosis for Electromechanical Equipment

Mathematical Problems in Engineering

Intelligent Monitoring, Diagnosis and Prognosis for Electromechanical Equipment

Lead Guest Editor: Zhi-Xin Yang
Guest Editors: Li-Jun Zhou, Xian-Bo Wang, and Om Prakash Yadav

Chief Editor

Academic Editors

Contents

Hindawi
Mathematical Problems in Engineering
Volume 2021, Article ID 9236726, 11 pages
https://doi.org/10.1155/2021/9236726

Research Article

Impact of the Field Winding Interturn Short-Circuit Position on Rotor Vibration Properties in Synchronous Generators

Xing-Hua Yuan,[1] **Yu-Ling He**,[1] **Man-Yu Liu**,[2] **Hui Wang**,[3] **Shu-Ting Wan**,[1] **and Gaurang Vakil**[4]

[1]*Department of Mechanical Engineering, Hebei Provincial Key Lab of Electric Power Equipment Maintenance and Failure Prevention, North China Electric Power University, Baoding 071003, China*
[2]*State Grid Beijing Electric Power Research Institute, Beijing 100000, China*
[3]*Department of Electrical Engineering, North China Electric Power University, Baoding 071003, China*
[4]*Department of Electrical and Electronics Engineering, University of Nottingham, NG7 2RD, Nottingham, UK*

Correspondence should be addressed to Yu-Ling He; heyuling1@163.com

Received 19 October 2021; Accepted 22 November 2021; Published 30 November 2021

Academic Editor: Xian-Bo Wang

This paper investigates the effect of the field winding interturn short-circuit (FWISC) position on the rotor vibration properties in turbo generators. Different from the previous studies which focused on the influence of the short-circuit degree, this work pays much attention to the impact of the short-circuit position on the rotor unbalanced magnetic pull (UMP) properties and vibration characteristics. The theoretical UMP model is firstly deduced based on the analysis of the magnetic flux density (MFD) variation. Then, the finite element analysis (FEA) is performed to calculate the UMP data. Finally, the rotor vibrations are tested on a CS-5 prototype generator which has two poles and a rated capacity of 5 kVA. It is shown that the occurrence of FWISC will greatly increase the UMP as well as the rotor vibration. In addition to the short-circuit degree, the short-circuit position will also affect the UMP and vibration. The nearer the short-circuit position is to the big rotor teeth, the larger the UMP and vibration will be. The proposed study in this paper will be beneficial for the monitoring and diagnosis of FWISC faults.

1. Introduction

Field winding interturn short circuit (FWISC) is a common electrical fault in synchronous generators and has been studied by scholars for a long time since the 1960s [1]. This fault can be caused due to many reasons [2] such as residual particles in the slot and the interturn insulation degrading. Luckily, it will not significantly affect the performance of the generator when the short-circuit degree is light. However, this fault will develop into an earth fault if without carrying out proper measures.

Scholars have made a lot of efforts in studying the electromagnetic properties. For instance, Dirani et al. studied the impact of the FWISC degree on the primary parameters such as the radial magnetic flux density (MFD), the radial force density, and the UMP of a 74 MVA industrial large hydrogenerator with 76 poles [3]. As a supplement, the authors of this paper have also studied the magnetic field variation due to FWISC, finding that both the short-circuit degree and the short-circuit position will affect MFD [4, 5] and the stator voltage/current [6]. It is found that the occurrence of FWISC will generally decrease the MFD [4, 5] and break the symmetric components of the stator voltage/current into asymmetric ones [6].

Besides the magnetic and the electrical parameters, scholars have also found that FWISC will still affect the frame/housing vibrations [7, 8] and the stator winding vibrations [9, 10]. Since the vibration and the electromagnetic torque are both in proportion to the square of the magnetic flux which can be considerable by FWISC, not only the

stator/housing vibration but also the electromagnetic torque will be influenced by such a fault. Typically, Hao et al. investigated the electromagnetic torque characteristics before and after FWISC [11], indicating that the torque ripples will be greatly strengthened by the interturn short circuit.

Based on the faulty electromagnetic properties, scholars and engineers have proposed various methods to monitor and diagnose the FWISC fault. For instance, Yucai and Yonggang calculated the difference between the virtual power and the actual electromagnetic power to detect the occurrence and the FWISC degree in turbine generators [12], while Hao et al. employed the rotor and the stator current to monitor the very fault based on multiloop theory [13]. To distinguish the rotor winding fault from the mechanical faults, Salomon et al. used the method of symmetrical components and proposed a simple, low-cost, and low intrusive condition monitoring system which only relied on stator electrical quantities [6], while more scholars alternatively employed the magnetic flux difference for pattern recognition [14].

It has been found that the saturable effect will affect the electromagnetic parameters due to its nonlinear effect [15]. As a typical technical method, Milasi et al. [16], Ehya and Nysveen [14], Yun et al. [17], and Yucai et al. [18] employed the noninvasive flux sensors to detect the FWISC fault in salient-pole [14, 16, 17] and nonsalient-pole synchronous generators [18], respectively, while Valavi et al. used the spectral analysis of stator voltage and current to diagnose the very fault [19]. Additionally, Li et al. used the circulating current inside the stator parallel branches to detect the interturn short circuit [20–22], while He et al. [23] and Wan et al. [22, 24] employed the stator and rotor vibrations to diagnose FWISC. To detect FWISC more quickly, intelligent methods such as digital neural network [25] are employed and have gained a satisfied effect.

The aforementioned studies have set up a good basis for the FWISC fault detection and monitoring. However, most of the studies primarily focus on the electromagnetic property variations due to the short-circuit degree, while the impact of the short-circuit position on the key electromechanical characteristics such as the rotor vibration has been rarely investigated in detail. As an improvement, in this paper, we focus on the rotor UMP and vibration properties under varied FWISC position cases in synchronous generators. Specifically, a nonsalient-pole prototype generator, which has two poles and a rated capacity of 5 kVA, is taken as the study object. The remainder of this paper is arranged as follows. Section 2 puts forward the theoretical analysis model of the rotor UMP, while Section 3 carries out the finite element analysis (FEA) and the experimental study on the CS-5 prototype generator to obtain the UMP values and the rotor vibrations for a validation. Finally, the main conclusions based on the theoretical analysis, FEA calculation, and experimental studies are drawn up in Section 4.

2. Theoretical Model

In turbo generators, the field winding is connected in series and embedded in the rotor slots, as indicated in Figures 1(a) and 1(b). As FWISC occurs, the exciting current I_f will no longer pass through the shorted turns, which means the current inside the shorted turns will be reduced to almost zero. Consequently, the rotor magnetomotive force (MMF) will be decreased due to the reduction of the exciting turns, as illustrated in Figure 1(c). Assuming that FWISC occurs in slot 1-1' (position 1) and 3-3' (position 2), respectively, with the same short-circuit turns, it is obvious that MMF will be decreased more in position 2 since α_{r2} is larger than α_{r1}. In Figure 1(c), the shadows represent the reduced amounts of MMF for the two different shorted position cases.

To concisely study the impact of FWISC on MMF, we add reversed I_f to the shorted turns so that the final current in these shorted turns can be turned to zero. Then, the analysis on the effect of the short circuit can be changed to the investigation on the impact of such a reversed current. According to the Gauss flux theorem, the positive magnetic flux produced by the reversed current should be equal to the negative magnetic flux, i.e., the yellow part in Figure 1(e) should have the same area as the green part. Then, the amplitudes of the yellow part and the green part can be calculated; see Figure 1(e), where n_m is the number of short-circuit turns. Finally, the rotor MMF will be changed from Figure 1(d) to Figure 1(f). More details about the calculation process can be found in [4].

As investigated in [4, 5], the rotor MMF F_r is $(90 + \psi)$ degree in front of the stator MMF F_s, as indicated in Figure 2(a), and the composite MMF can be written as

$$\begin{cases} f(\alpha_m, t) = F_s \cos(\omega t - \alpha_m - \psi - 0.5\pi) + F_r \cos(\omega t - \alpha_m) = F_c \cos(\omega t - \alpha_m - \beta) \\ F_c = \sqrt{F_s^2 \cos^2 \psi + (F_r - F_s \sin \psi)^2} \\ \beta = \arctan \dfrac{F_s \cos \psi}{F_r - F_s \sin \psi} \end{cases}, \quad (1)$$

where α_m is the mechanical angle to indicate the circumferential position of the air gap, ω is the electrical angular frequency (for turbo generators, it is equal to the mechanical angular frequency of the rotor ω_r), ψ is the internal power angle of the generator, and F_c is the vector summation of F_s and F_r. Since the occurrence of FWISC decreases F_r, the

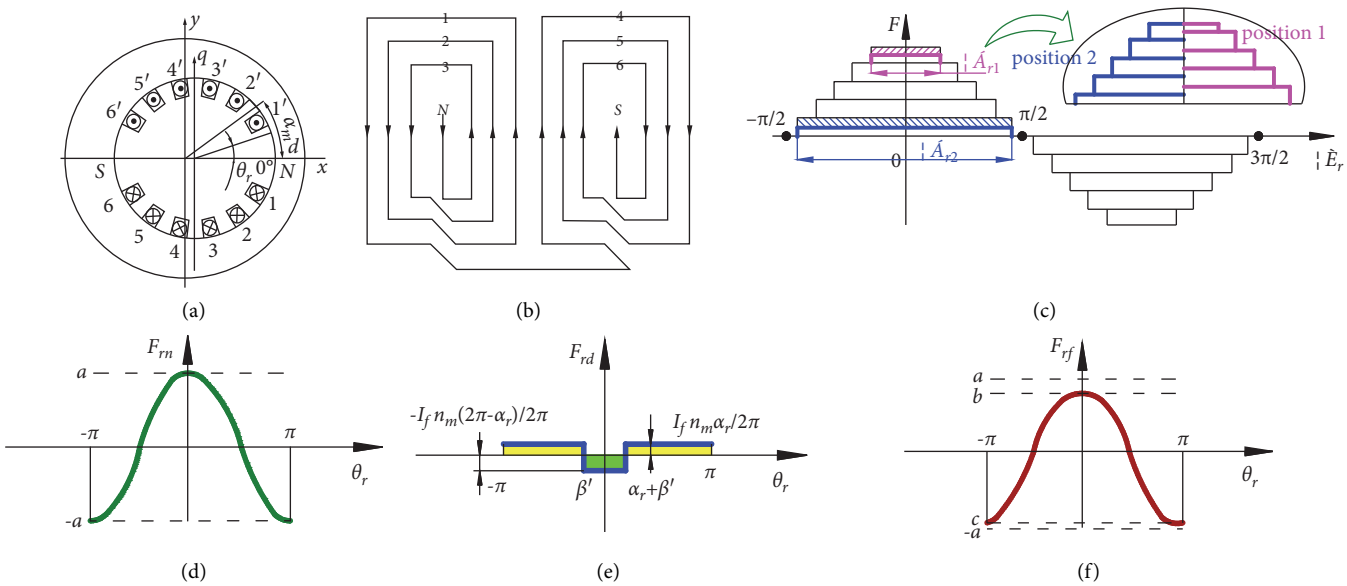

Figure 1: Rotor MMF variation: (a) rotor structure, (b) field winding connection, (c) MMF reduction due to FWISC in two different positions, (d) normal rotor MMF, (e) inversed MMF by short-circuit turns, and (f) MMF after FWISC.

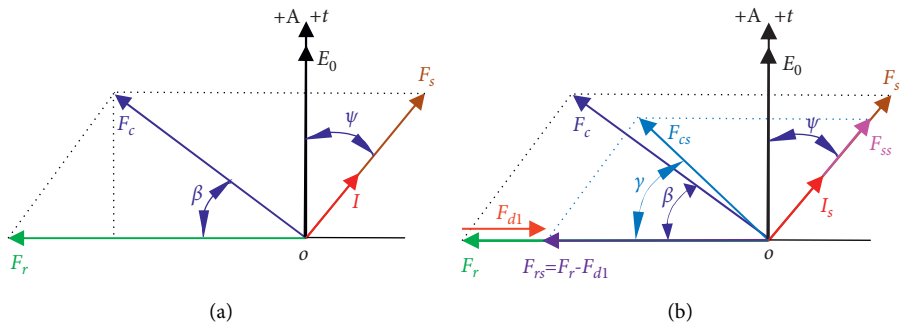

Figure 2: Fundamental frequency MMFs (a) before and (b) after FWISC.

stator MMF will also be reduced, as illustrated in Figure 2(b). Consequently, the composite MMF will be decreased from F_c to F_{cs}.

Since different MMF harmonics (both the rotor MMF and the stator MMF) rotate at varied speeds, for the sake of clarification, in Figure 2, all of the MMFs are the 1st ones. The higher-order harmonics have the similar situation as the 1st ones and therefore are not illustrated in this figure due to the limitation of the space. In Figure 2(b), F_{d1} is the 1st harmonic of the inversed MMF produced by the short-circuit turns, and it can be obtained based on the performance of Fourier series decomposition.

Then, the composite MMF illustrated in Figure 2(b) can be written as

$$f(\alpha_m, t) = F_{ss}\cos(\omega t - \alpha_m - \psi - 0.5\pi) + (F_r - F_{d1})\cos(\omega t - \alpha_m) = F_{cs}\cos(\omega t - \alpha_m - \gamma). \quad (2)$$

To indicate the short-circuit position, the angle between the two slots where FWISC takes place is employed; see α_r in Figures 1(c) and 1(e). The larger value of α_r indicates that the short-circuit position moves away farther from the big tooth of the rotor. Qualitatively, the larger α_r is, the larger F_{d1} will be, but, on the contrary, the smaller F_{cs} will be.

The unbalanced magnetic pull (UMP) on the rotor can be obtained via [22, 24].

$$\begin{cases} F_X = \mathrm{LR}\int_0^{2\pi} q(\alpha_m, t)\cos\ \alpha_m \,\mathrm{d}\alpha_m \\ F_Y = \mathrm{LR}\int_0^{2\pi} q(\alpha_m, t)\sin\ \alpha_m \,\mathrm{d}\alpha_m \\ q(\alpha_m, t) = \dfrac{B^2(\alpha_m, t)}{2\mu_0} \\ B(\alpha_m, t) = f(\alpha_m, t)\Lambda_0 \end{cases}, \tag{3}$$

where F_X and F_Y are the UMPs in the X (horizontal) direction and the Y (vertical) direction, respectively, q is the magnetic pull per unit area, B is the magnetic flux density (MFD), and Λ_0 is the permeance per unit area.

Feed (1) and (2) into (3), respectively; the rotor UMP in normal and FWISC cases can be written as

$$\begin{cases} F_X = \begin{cases} 0 \ldots\ldots \text{normal} \\ \dfrac{-F_{Cs}F_{d2}LR\Lambda_0^2\pi}{2\mu_0}\cos(\omega t + \gamma - 2\varphi_2) \ldots \text{FWISC} \end{cases} \\ F_Y = \begin{cases} 0 \ldots\ldots \text{normal} \\ \dfrac{-F_{Cs}F_{d2}LR\Lambda_0^2\pi}{2\mu_0}\sin(\omega t + \gamma - 2\varphi_2) \ldots \text{FWISC} \end{cases} \end{cases}, \tag{4}$$

where F_{d2} is the 2nd harmonic of the reversed MMF produced by the short-circuit turns, F_{cs} is the composite MMF in the FWISC case (see Figure 2(b)), and φ_2 is the angle between F_{d2} and the X-axis.

According to (4), the occurrence of FWISC will bring in the extra 1st UMP harmonic to the rotor, resulting in the intensified vibration at ω. Moreover, it is suggested from Figure 1(c), Figure 2(b), and equation (3) that the increment of α_r will decrease F_{cs} and B. Consequently, the UMPs F_X and F_Y will also be decreased. Briefly, for the rotor UMP and vibration, the nearer short-circuit position to the big tooth with the same short-circuit degree has the similar effect as the severer short-circuit degree at the same shorted position. The short-circuit degree is defined as

$$f\ d = \frac{n_m}{N} \times 100\%, \tag{5}$$

where n_m is the number of short-circuit turns, while N is the number of total exciting turns.

3. FEA and Experimental Study

3.1. FEA and Experimental Setup. FEA and experiments are carried out on a CS-5 prototype generator in the State Key Laboratory of Alternate Electrical Power Systems with Renewable Energy Sources, P. R. China, as illustrated in Figure 3(a). The prototype generator has two poles and a rated rotating speed of 3000 rpm. The primary parameters of the prototype generator are listed in Table 1.

On the generator, there is a plate with several interturn short-circuit taps for the field windings, as shown in Figure 3(a). During the experiment, L_0-L_1, L_1-L_2, and L_2-L_3 are connected, respectively, to simulate 5% FWISC at varied positions. Two PCB accelerometers with very little volume and mass are fixed to the horizontal direction and the vertical direction of the bearing block, respectively, to test the vibration signals of the rotor, as shown in Figure 3(b).

2D FEA is carried out, with the parameter settings the same as the experimental ones. The finite element models are illustrated in Figure 3(c), while the external coupling circuit models are shown in Figure 3(d). During FEA, four groups of calculations are carried out:

(1) Normal condition: no FWISC is set, as illustrated in the first figure in Figure 3(c). The data are collected as the reference for further comparison with the faulty cases.

(2) 5% FWISC at position 1 with minimal α_r (hereafter, it is written as FWISC5%-1), as illustrated in the second figure in Figure 3(c).

(3) 5% FWISC at position 2 (hereafter, it is written as FWISC5%-2), as illustrated in the third figure in Figure 3(c).

(4) 5% FWISC at position 3 with maximal α_r (hereafter, it is written as FWISC5%-3), as illustrated in the fourth figure in Figure 3(c).

The aforementioned four cases are also carried out for at least three times in the experiment, respectively, to get sufficient test data. The experimental results show a general consistency, with only small value variations in the vibration amplitudes. More details about the FEA data and the experimental results can be specifically found in Section 3.2.

3.2. Results and Discussion. The MFD and the phase current variations before and after FWISC are illustrated in Figures 4(a) and 4(b), respectively. It is shown that MFD and the phase current at FWISC cases will have smaller amplitudes than the normal condition. As the short circuit goes away from the big tooth, namely, α_r increases, MFD as well as the phase current will be decreased. The larger α_r is, the more MFD/current will be decreased. Such a result is consistent with Figures 1(c)–1(f).

The UMPs in the X-direction and Y-direction by FEA are illustrated in Figures 5(a) and 5(b), respectively, while the tested vibrations in X- and Y-directions are indicated in Figures 6(a) and 6(b), respectively. It is shown that, as the short-circuit position moves away from the big tooth, namely, α_r goes bigger, the UMPs in both X-direction and Y-direction will be decreased. Correspondingly, the rotor vibrations in X- and Y-directions will also be decreased. The very reason is that the magnetic pull is in proportion to MFD, as indicated in equation (3); bigger α_r will make MFD to decrease more, as illustrated in Figures 1(c) and 1(e). Although the rotor UMPs and the vibrations will be decreased as the increment of α_r, they are still larger than those in the normal condition since the occurrence of FWISC will break down the magnetic pull balance between the two poles.

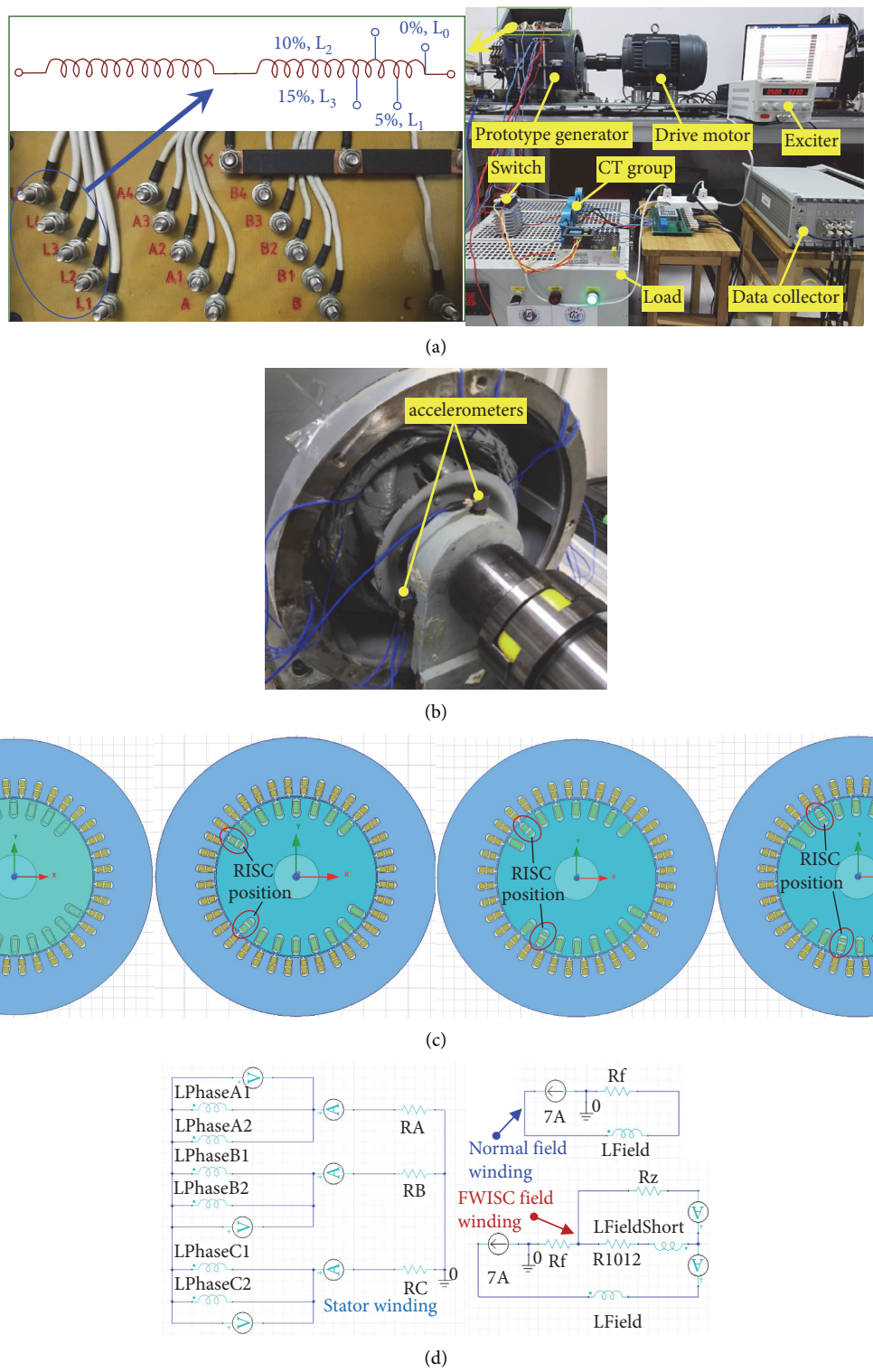

Figure 3: Experiment and FEA setup on a CS-5 prototype generator: (a) picture of the generator set, (b) accelerometers' setup for the rotor vibration test, (c) FE models: from left to right, for normal condition and FWISC cases at position 1, 2, and 3, respectively, and (d) external coupling winding circuits.

The UMP and the vibration spectra are shown in Figures 5(c) and 5(d) and Figures 6(c) and 6(d), respectively. As indicated in Figures 5(c) and 5(d), the primary UMP components are the odd harmonics, primarily the 1st, 5th, and 7th. Such a result is in good accordance with equation (4). In equation (4), the UMP result mainly takes into account the interaction between the 1st composite MMF and the 2nd inversed MMF harmonic (F_{d2}), while actually, there are still

Table 1: Key parameters of the CS-5 prototype generator.

Parameter	Value
Rated capacity	5 KVA
Rated voltage	380 v
Rated rotating speed	3000 rpm
Number of pole pairs	1
Connection mode of the stator winding	2 Y
Pitch	14
Number of stator slots	36
Power factor	0.8
Number of rotor slots	16
Number of turns per rotor slot	60
Outer diameter of the rotor	142.6 mm
Inner diameter of the stator	145 mm
Rated stator current	7.6 A
Length of the stator and rotor	130 mm

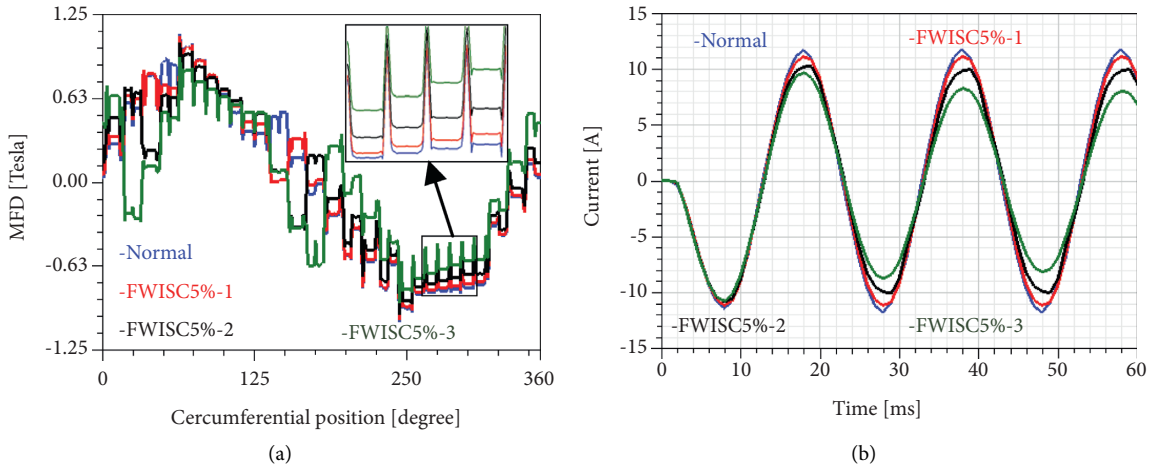

Figure 4: MFD and current variations for FWISC cases with varied short-circuit positions: (a) MFD and (b) phase current.

other odd composite MMF harmonics such as the 3rd, 5th, and 7th harmonics. Consequently, the square operation in equation (3) will produce odd UMP harmonics. However, for the experimental vibration spectra, the cases are much more complex. As indicated in Figures 6(c) and 6(d), the rotor vibrations still have even harmonics in addition to the odd harmonics since the stator vibrations (mainly even harmonics) will be transferred to the rotor through the foundation and the bearings [23]. It is also suggested from Figure 6 that there are some asymmetric factors inside the generator since the rotor has vibrations of each harmonic in even normal condition. The vibration spectra in the X-direction do not strictly follow the theoretical developing tendency since vibration is a complex phenomenon which can be affected by many factors. However, the vibrations in the Y-direction present a much better result. Theoretically, the 3rd vibration harmonic should not have that large amplitude; please see Figures 6(c) and 6(d). The authors have repeated the experiments for several times but generally obtained similar data. After comprehensive analysis and test, it is found that the bearing blocks have a natural frequency at about 150 Hz.

To more vividly present the action of the UMP on the rotor, the force distributions by FEA are illustrated in Figure 7. It is shown that, in the normal condition, the magnetic forces at the two poles are generally symmetric, as indicated in Figure 7(a). However, the occurrence of FWISC will break down such symmetry. As α_r goes bigger, namely, the short-circuit position goes farther away from the big tooth, the amplitude of the edge force will be decreased, but the general UMP (difference value of the summing edge force between two sides) on the whole rotor will be increased. Such a result is consistent with the aforementioned analysis.

Since the vibration is actually the periodic deformation/movement with respect to a central position, the rotor deformation/movement amplitude represents the vibration amplitudes. We also carry out a quick calculation to obtain the rotor deformation under the action of the UMPs. During the calculation, we perform the approximated constraint and load on the rotor. Physically, the rotor is restrained by the bearings. However, since we carry out a 2D FEA in which it is hard to simulate the fix effect of the bearings in two different axial positions, we approximately fix the rotor on one side and apply the UMP on the other side, as illustrated in Figure 8(a).

The rotor deformation results at the same moment are illustrated in Figures 8(b)–8(e). Since this is an equivalent fast calculation, the deformation result may not be so

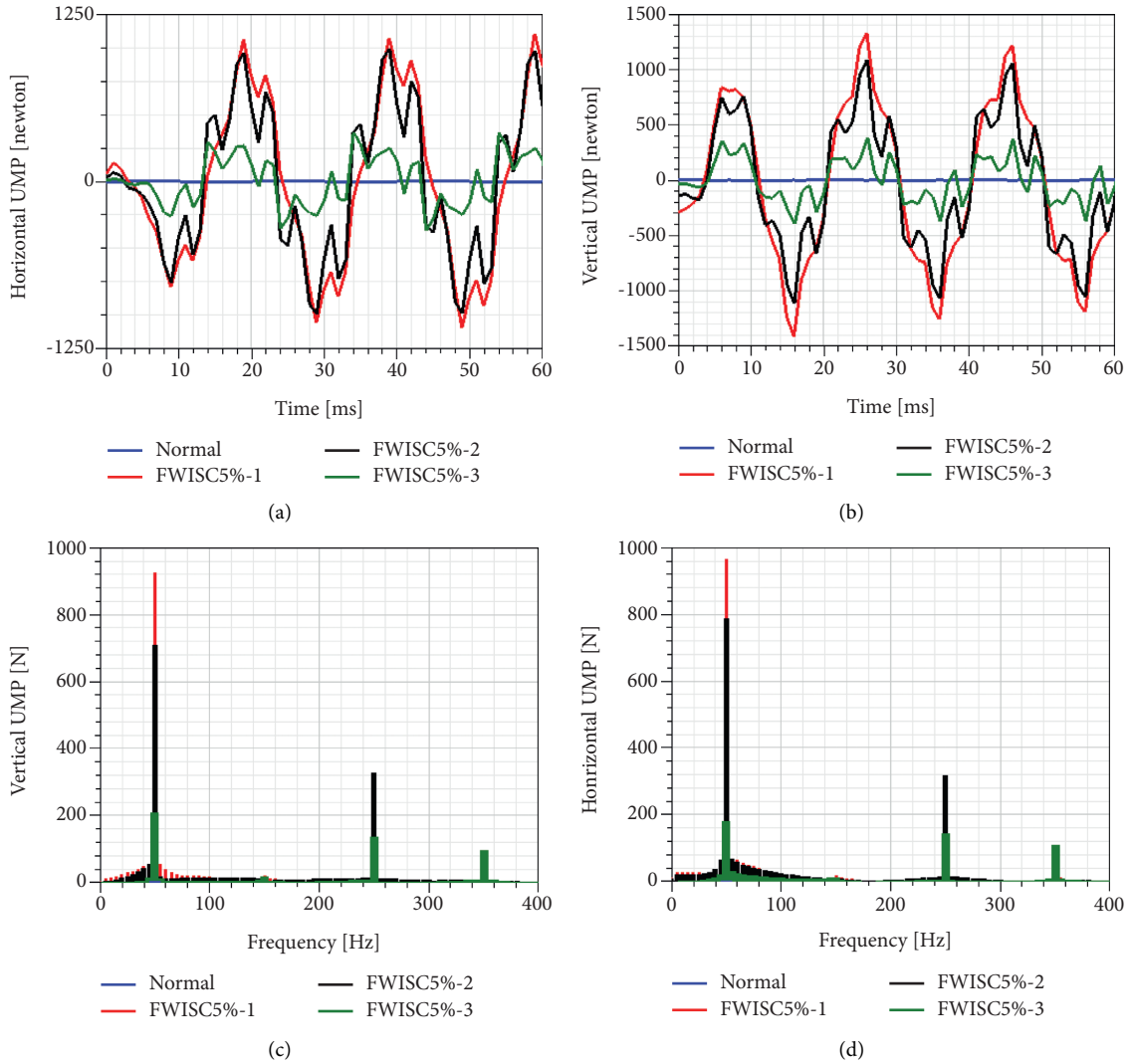

Figure 5: UMPs by FEA: (a) X-direction curves, (b) Y-direction curves, (c) X-direction spectrum, and (d) Y-direction spectrum.

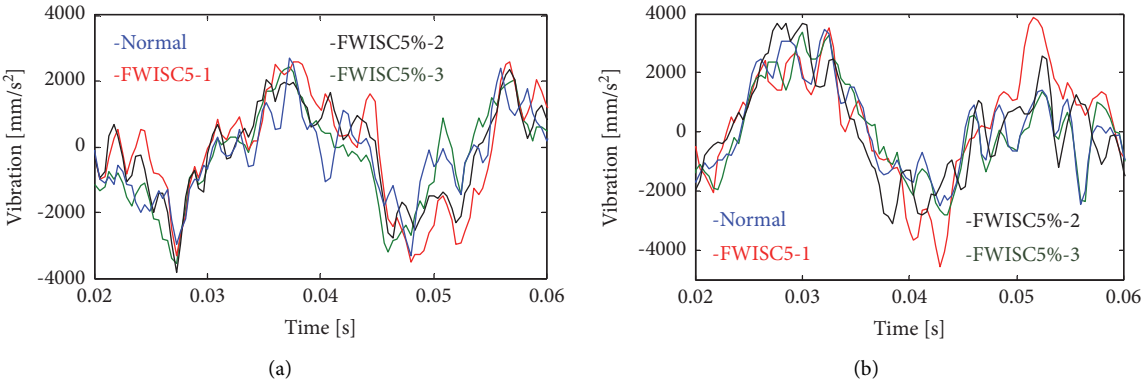

Figure 6: Continued.

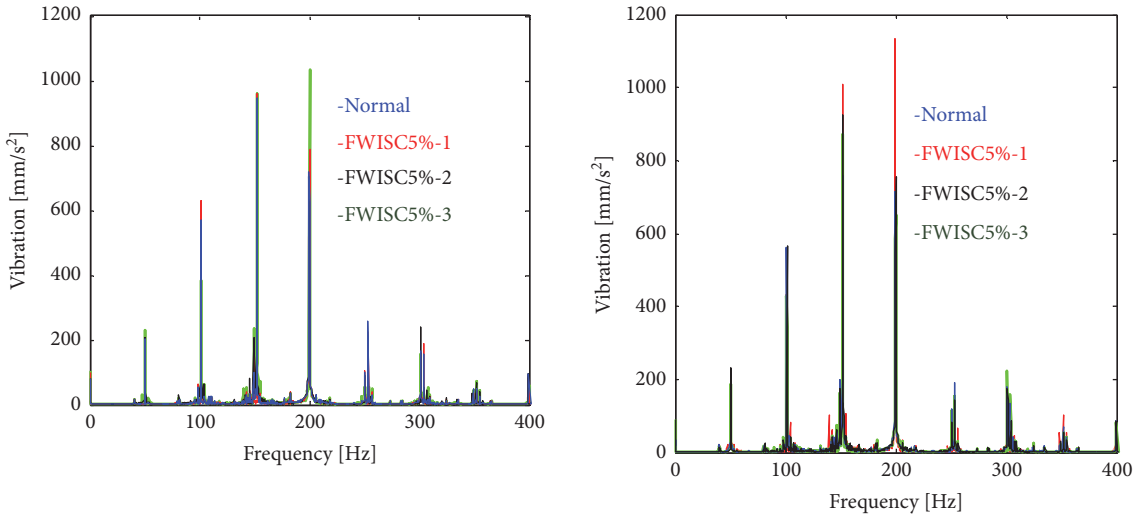

Figure 6: Vibrations by experiment: (a) X-direction curves, (b) Y-direction curves, (c) X-direction spectrum, and (d) Y-direction spectrum.

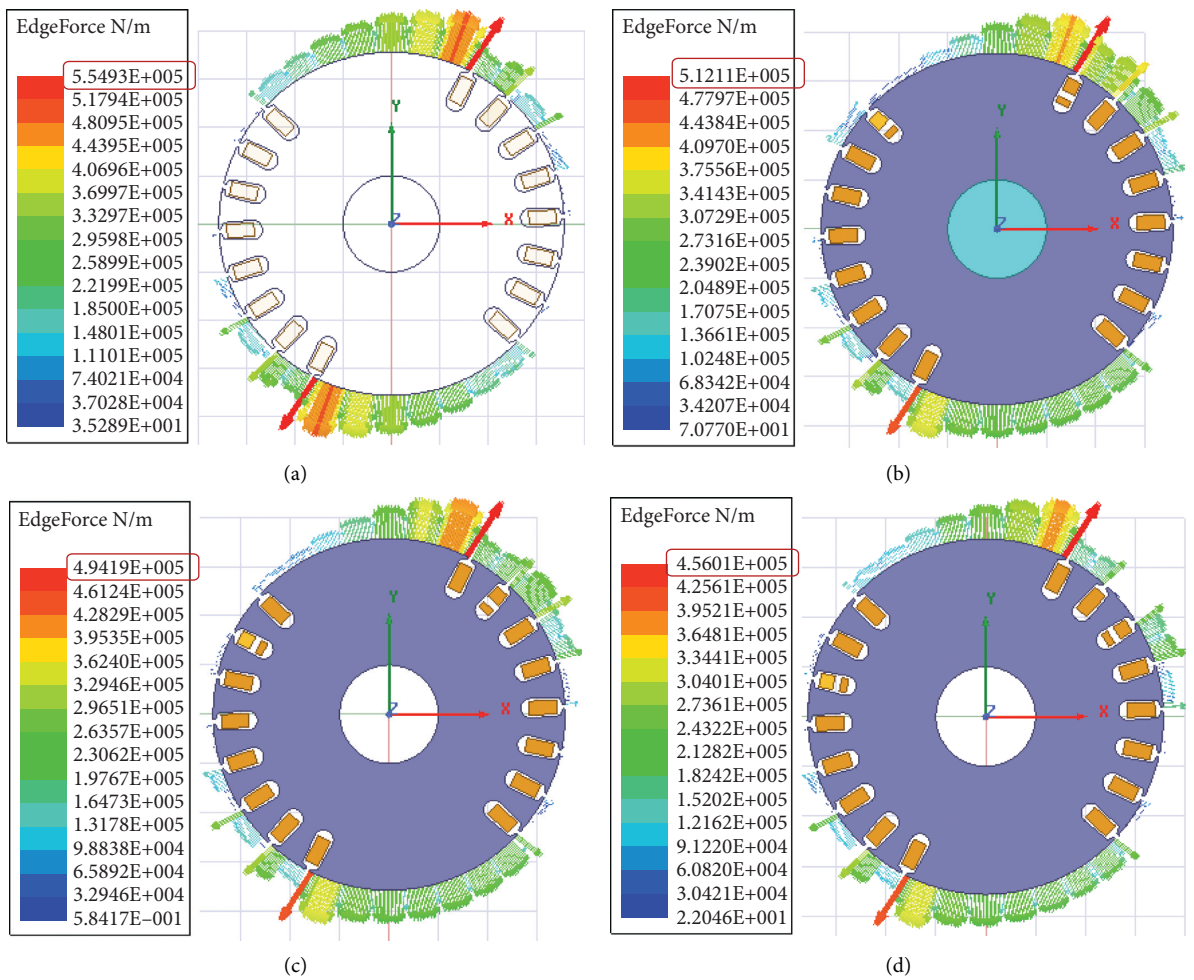

Figure 7: Edge force distribution at 0.2 s: (a) normal and (b–d) 5% FWISC at position 1, 2, and 3, respectively.

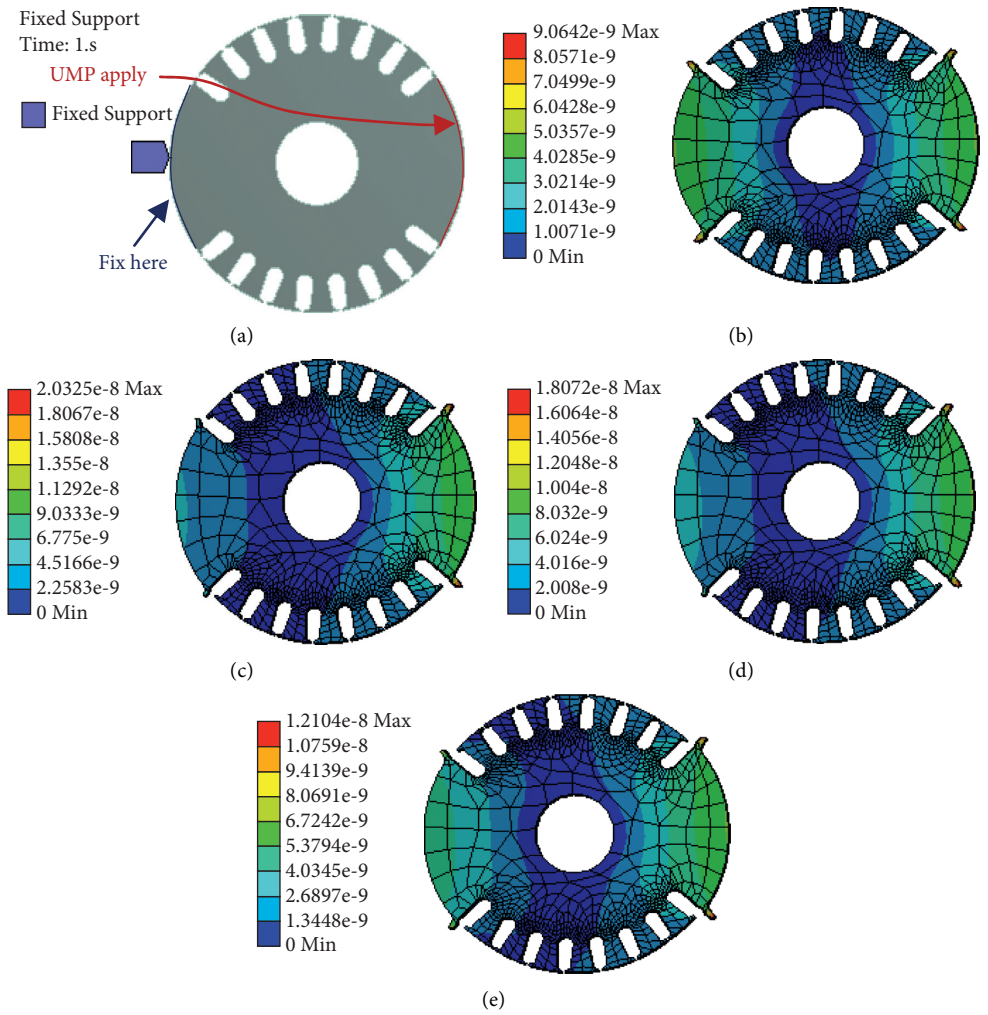

Figure 8: Max deformation by FEA: (a) detailed fix position and UMP apply position, (b) normal deformation, and (c–e) deformation in 5% FWISC cases at position 1, 2, and 3, respectively.

accurate, but the deformation tendency should be the same as the practical one. It shows that, in FWISC cases, the rotor will have a larger deformation than in the normal condition. As the short-circuit position goes farther away from the big tooth, the deformation amplitude will be decreased, indicating that the rotor vibration magnitudes will be reduced. Such a trend follows the previous analysis well.

4. Conclusions

This paper investigates the impact of the field winding interturn short-circuit position on the rotor UMPs and vibrations. The whole work is based on the theoretical analysis, the finite element calculation, and the experimental test. The primary contribution of this paper mainly lies in two aspects: (1) the influence of the FWISC position on MFD and the exact way about how such an influence takes place are comprehensively studied, while other research studies mainly focused on the impact of FWISC degrees; (2) the impact of the FWISC position on the rotor UMPs and vibrations is investigated, finding out the UMP/vibration developing tendency/regularity, while other scholars have rarely paid attention to this field.

The primary conclusions based on the study proposed in this work can be drawn up as follows:

(1) Normally, the rotor UMP is very little due to the symmetric distribution of the magnetic force.

(2) The occurrence of FWISC will increase the rotor UMPs in both X- and Y-directions. Consequently, the rotor vibrations in these two directions will be amplified.

(3) As the FWISC position goes farther away from the big tooth, the rotor UMPs as well as the rotor vibrations will be decreased, but are still larger than those in the normal condition.

Since the findings in this paper include the rotor UMP/vibration developing regularity due to varied FWISC positions, they are highly potential to be employed as a supplement to the current knowledge base and will be beneficial for the condition monitoring and the failure prevention in turbo generators. Moreover, the aforementioned study

results can also be extended to other similar generators that have wound rotors, regardless of the pole numbers. For instance, the conclusion can be applied to the hydrogenerators which have multi-salient-poles and the nuclear turbine generators which have two nonsalient-pole pairs.

Data Availability

The data used to support the findings of this study are available from the corresponding author upon request.

Conflicts of Interest

All of the authors declare that there are no conflicts of interest regarding the publication of this paper.

Acknowledgments

This work was supported by the National Natural Science Foundation of China (51777074), the Chinese Fundamental Research Funds for the Central Universities (2017MS151), the Hebei Provincial Natural Science Foundation (E2020502032), and the Top Youth Talent Support Program of Hebei Province ([2018]-27).

References

[1] P. Hermann, R. Mahrt, and H. Doon, "Detecting and locating interturn short circuits on turbine-generator rotors," *IEEE Transactions on Power Apparatus and Systems*, vol. 82, no. 68, pp. 686–698, 1963.

[2] D. Albright, "Interturn short-circuit detector for turbine-generator rotor windings," *IEEE Transactions on Power Apparatus and Systems*, vol. PAS-90, no. 2, pp. 478–483, 1971.

[3] H. C. Dirani, A. Merkhouf, B. Kedjar, A.-M. Giroux, and K. Al-Haddad, "Rotor interturn short circuit impact on large hydrogenerator magnetic quantities," *IEEE Transactions on Industry Applications*, vol. 54, no. 4, pp. 3702–3711, 2018.

[4] Y.-L. He, M.-Q. Ke, G.-J. Tang, H.-C. Jiang, and X.-H. Yuan, "Analysis and simulation on the effect of rotor interturn short circuit on magnetic flux density of turbo-generator," *Journal of Electrical Engineering*, vol. 67, no. 5, pp. 323–333, 2016.

[5] Y.-L. He, Y. Wang, H.-C. Jiang et al., "A novel universal model considering SAGE for MFD-based faulty property analysis under RISC in synchronous generators," *IEEE Transactions on Industrial Electronics*, p. 1, 2021.

[6] C. P. Salomon, W. C. Santana, G. Lambert-Torres et al., "Discrimination of synchronous machines rotor faults in electrical signature analysis based on symmetrical components," *IEEE Transactions on Industry Applications*, vol. 53, no. 3, pp. 3146–3155, 2017.

[7] M. Cuevas, R. Romary, J.-P. Lecointe, and T. Jacq, "Non-invasive detection of rotor short-circuit fault in synchronous machines by analysis of stray magnetic field and frame vibrations," *IEEE Transactions on Magnetics*, vol. 52, no. 7, pp. 1–4, 2016, 8105304.

[8] M. Cuevas, R. Romary, J.-P. Lecointe, F. Morganti, and T. Jacq, "Noninvasive detection of winding short-circuit faults in salient Pole synchronous machine with squirrel-cage damper," *IEEE Transactions on Industry Applications*, vol. 54, no. 6, pp. 5988–5997, 2018.

[9] G.-J. Tang, H.-C. Jiang, Y.-L. He, and Q.-F. Meng, "Electromagnetic forces and mechanical responses of stator windings before and after rotor interturn short circuit in synchronous generators," *Mathematical Problems in Engineering*, vol. 2020, pp. 1–19, Article ID 5892312, 2020.

[10] Q. Meng and Y. He, "Mechanical response before and after rotor inter-turn short-circuit fault on stator windings in synchronous generator," in *Proceedings of the 2018 IEEE Student Conference on Electric Machines and Systems*, pp. 1–7, Huzhou, China, December 2018.

[11] L. Hao, J. Wu, and Y. Zhou, "Theoretical analysis and calculation model of the electromagnetic torque of nonsalient-Pole synchronous machines with interturn short circuit in field windings," *IEEE Transactions on Energy Conversion*, vol. 30, no. 1, pp. 110–121, 2015.

[12] W. Yucai and L. Yonggang, "Diagnosis of rotor winding interturn short-circuit in turbine generators using virtual power," *IEEE Transactions on Energy Conversion*, vol. 30, no. 1, pp. 183–188, 2015.

[13] L. Hao, Y. Sun, A. Qiu, and X. Wang, "Steady-state calculation and online monitoring of interturn short circuit of field windings in synchronous machines," *IEEE Transactions on Energy Conversion*, vol. 27, no. 1, pp. 128–138, 2012.

[14] H. Ehya and A. Nysveen, "Pattern recognition of interturn short circuit fault in a synchronous generator using magnetic flux," *IEEE Transactions on Industry Applications*, vol. 57, no. 4, pp. 3573–3581, 2021.

[15] P. Naderi and A. Shiri, "Rotor/stator inter-turn short circuit fault detection for saturable wound-rotor induction machine by modified magnetic equivalent circuit approach," *IEEE Transactions on Magnetics*, vol. 53, no. 7, pp. 1–13, 2017.

[16] M. E. Milasi, S. Afrandideh, and F. Haghjoo, "A simple flux-based technique to specify the faulty Pole of the salient Pole synchronous machines," *IEEE Transactions on Energy Conversion*, vol. 36, no. 1, pp. 264–271, 2021.

[17] J. Yun, S. Park, C. Yang et al., "Comprehensive monitoring of field winding short circuits for salient Pole synchronous motors," *IEEE Transactions on Energy Conversion*, vol. 34, no. 3, pp. 1686–1694, 2019.

[18] W. Yucai, M. Qianqian, and C. Bochong, "Fault diagnosis of rotor winding inter-turn short circuit for sensorless synchronous generator through screw," *IET Electric Power Applications*, vol. 11, no. 8, pp. 1475–1482, 2017.

[19] M. Valavi, K. G. Jorstad, and A. Nysveen, "Electromagnetic analysis and electrical signature-based detection of rotor inter-turn faults in salient-Pole synchronous machine," *IEEE Transactions on Magnetics*, vol. 54, no. 9, pp. 1–9, 2018.

[20] Y.-G. Li, Y.-J. Zhao, L. Chen, and X. Ji, "Fault diagnosis of rotor winding inter-turn short circuit in turbine-generator based on BP neural network," in *Proceedings of the 2008 International Conference on Electrical Machines and Systems*, pp. 783–787, Wuhan, China, October 2008.

[21] Y. Li, Y. Sun, L. Wang, and H. Li, "The criterion on inter-turn short circuit fault diagnose of steam turbine generator rotor windings," in *Proceedings of the 2007 International Conference on Electrical Machines and Systems (ICEMS)*, pp. 1050–1054, Seoul, Republic of Korea, October 2007.

[22] W. Shuting, L. Yonggang, L. Heming, and T. Guiji, "A compositive diagnosis method on turbine-generator rotor winding inter-turn short circuit fault," in *Proceedings of the 2006 IEEE International Symposium on Industrial Electronics*, pp. 1662–1666, Montreal, Canada, July 2006.

[23] Y.-L. He, W.-Q. Deng, B. Peng et al., "Stator vibration characteristic identification of turbogenerator among single and composite faults composed of static air-gap eccentricity

and rotor interturn short circuit," *Shock and Vibration*, vol. 2016, Article ID 5971081, 14 pages, 2016.

[24] S. Wan, Y. Li, H. Li, and G. Tang, "The new diagnosis method of rotor winding inter-turn short circuit fault and imbalance fault based on stator and rotor vibration characteristics," in *Proceedings of the 2005 International Conference on Electrical Machines and Systems*, vol. 3, pp. 2207–2210, Nanjing, China, September 2005.

[25] S. Toma, L. Capocchi, and G.-A. Capolino, "Wound-rotor induction generator inter-turn short-circuits diagnosis using a new digital neural network," *IEEE Transactions on Industrial Electronics*, vol. 60, no. 9, pp. 4043–4052, 2013.

Hindawi
Mathematical Problems in Engineering
Volume 2021, Article ID 9589412, 10 pages
https://doi.org/10.1155/2021/9589412

Research Article

Research on the Noise Reduction Method of the Vibration Signal of the Hydrogenerator Unit Based on ITD-PE-SVD

Yan Ren,[1,2] **Pan Liu**,[1] **Leiming Hu**,[3] **Ruoyu Qiao**,[1] **Linlin Zhang**,[1] **and Shaojie Huang**[4]

[1]*School of Electric Power, North China University of Water Resources and Electric Power, Zhengzhou 450045, China*
[2]*Hunan Provincial Key Laboratory of Renewable Energy Power Technology (Changsha University of Science and Technology), Changsha 410114, China*
[3]*Jiangxi Hongping Pumped Storage Co., Ltd., Yichun 330600, China*
[4]*Henan Nuclear Industry Radionuclide Testing Center, Zhengzhou 450046, China*

Correspondence should be addressed to Yan Ren; renyan@ncwu.edu.cn and Pan Liu; 773793250@qq.com

Received 4 August 2021; Accepted 25 August 2021; Published 8 September 2021

Academic Editor: Xian-Bo Wang

Aiming at the problem that the vibration signals of the hydrogenerator unit are nonlinear and nonstationary and it is difficult to extract the signal features due to strong background noise and complex electromagnetic interference, this paper proposes a dual noise reduction method based on intrinsic time-scale decomposition (ITD) and permutation entropy (PE) combined with singular value decomposition (SVD). Firstly, the vibration signals are decomposed by ITD to obtain a series of PRC components, and the permutation entropy of each component is calculated. Secondly, according to the set permutation entropy threshold, the PRC components are selected for reconstruction to achieve a noise reduction effect. On this basis, SVD is carried out, and the appropriate reconstruction order is selected according to the position of the singular value difference spectrum mutation point for reconstruction, so as to achieve the secondary noise reduction effect. The proposed method is compared with the LMD-PE-SVD and EMD-PE-SVD dual noise reduction method by simulation, taking the correlation coefficient and signal-to-noise ratio to evaluate the noise reduction performance and finding that the ITD-PE-SVD noise reduction has good noise reduction and pulse effect. Furthermore, this method is applied to the analysis of the upper guide swing data in the X-direction and Y-direction of a unit in a hydropower station in China, and it is found that this method can effectively reduce noise and accurately extract signal features, thus determining the vibration cause, which is helpful to improve the turbine fault recognition rate.

1. Introduction

As a clean and renewable energy, hydropower has mature development technology, which meets the needs of China's energy strategic development. As the core equipment of hydropower energy conversion, the operation state of hydropower units directly affects the efficiency of energy conversion. If an abnormality or failure occurs, it will lead to the reduction of power transmission quality and the disturbance of power grid frequency, endangering the safety and stability of units and power plants. In severe cases, it will cause huge economic losses and casualties. Therefore, the stability of its operation has always been the focus of research. Due to the nonlinearity and nonstationarity of the signal are more intense when the hydropower unit is in unsteady operation, and at the same time, due to the influence of strong background noise and complex electromagnetic interference, the collected signal contains larger noise components, thus affecting the accurate extraction of vibration signal features. In the practical engineering application of unit condition monitoring and fault diagnosis, in order to extract the most representative fault features and improve the accuracy of diagnosis and analysis, the key first step is to process vibration signals. Therefore, the effective noise reduction of the collected vibration signals is of great significance to accurately judge the fault function of the unit.

At present, there are many methods for nonstationary signal processing, such as short-time Fourier transform

(STFT) [1], wavelet transform (WT) [2], empirical mode decomposition (EMD) [3], and local mean decomposition (LMD) [4]. The basic idea of short-time Fourier transform is to realize the quasi-stationary performance of nonstationary signal through time window function and then obtain the time-varying law of signal frequency domain characteristics. As a generalization of Fourier transform, this method retains the characteristics of linear transformation and has good effect in processing quasi-stationary signals, but it is not ideal for processing nonstationary signals [5–7]. Wavelet transform inherits and expands the localization idea of STFT, effectively overcomes the defect of fixed window area, and can focus on arbitrary details of signals, which is a real multiresolution analysis and is widely used. However, its noise reduction performance is greatly affected by the selection of wavelet bases, and there is no unified standard for selecting wavelet bases at present [8–10]. Aiming at the shortcomings of wavelet transform, the scholars have proposed EMD analysis methods [11, 12], which can adaptively decompose the signal into a series of IMF components with definite frequency amplitude according to the time domain characteristics of the signal itself. However, the EMD decomposition can easily lead to modal aliasing and large iterative computation [12, 13]. The adaptive signal decomposition method of local mean decomposition proposed in [4] can overcome the defects of EMD method after improvement, and the iteration times and operation speed are better than EMD, but the problem of modal aliasing has not been fundamentally solved [14–16]. In addition, considering the complexity of the real signal and its application in practical engineering, it is more effective to extract the useful signals from strong interference by using the hybrid method than by using one method alone [17–19].

Based on the above analysis, aiming at the problem that it is difficult to extract the vibration signal characteristics of hydrogenerator units under the background of strong noise and complex electromagnetic interference, combined with the advantages of inherent time-scale decomposition, permutation entropy and singular value, a dual noise reduction method based on ITD-PE-SVD is proposed. Intrinsic time-scale decomposition (ITD) is an adaptive signal time-frequency analysis method proposed by Frei et al. in 2007 [20, 21]. This method decomposes the nonstationary complex signal into a series of intrinsic rotation components (PRC) and a residual trend component (RTC), which overcomes the edge effect of EMD and weakens the mode mixing and other phenomena. The calculation speed is significantly improved compared with EMD and LMD, and the feature information of nonstationary can be extracted more accurately and efficiently [22, 23]. The permutation entropy (PE) is an algorithm for measuring the complexity of time series. Compared with sample entropy and approximate entropy, it has the advantages of simple calculation process, prominent anti-interference ability, and more sensitive to mutation signals. It can be used to deal with the problems of complex vibration signal components and weak fault signal of hydropower units [24–26]. Singular value decomposition (SVD) is based on matrix decomposition and transformation; it decomposes the signal into the superposition of a series of linear components and has the advantages that the waveform is not easy to be distorted, and the zero-phase shift is small. It can effectively detect the weak information mutation in the signal under complex background and has outstanding effect in feature information extraction and noise reduction [27–29].

Therefore, the ITD-PE-SVD proposed in this paper combines the advantages of the above three algorithms, so as to realize the dual noise reduction of the vibration signal of the unit under the background of strong noise and complex electromagnetic interference and accurately extract the weak fault feature information of the unit, so as to accurately determine the vibration reason of the unit and provide theoretical basis for the subsequent fault diagnosis.

The first part of this paper describes the principle of this noise reduction method, the second part uses this method to carry out simulation and comparative analysis, and the third part selects the upper guide swing data in X-direction and Y-direction of a hydropower station in China for example verification. Finally, the application of this method in vibration signal feature extraction of hydrogenerator units under strong noise background is summarized and prospected.

2. Principle of the ITD-PE-SVD Method

2.1. Principle of Inherent Time-Scale Decomposition. The ITD adaptively decomposes nonlinear nonstationary signals into multiple proper rotation components (PRC) and a residual trend component (RTC). The main idea of constructing the baseline signal is to perform linear transformation between any two adjacent maximum or minimum signal segments [20–22].

Suppose the fault signal X_t, $t = 0, 1, 2$, L is defined as the baseline extraction operator and the decomposition process is expressed as follows:

$$X_t = LX_t + (1 - L)X_t = L_t + H_t. \tag{1}$$

L_t is the baseline component and contains local relatively low frequency information in the fault signal; H_t is the appropriate rotational component and contains the local relative high-frequency information in the fault signal.

Remove the high-frequency rotating component after one decomposition, then take the baseline component signal as the next signal to be decomposed, and finally iterate the above decomposition process until the monotone trend component signal shows trouble signal X_t. The whole decomposition process of X_t is defined as follows:

$$\begin{aligned} X_t &= HX_t + LX_t = HX_t + (H + L)LX_t \\ &= \left(H \sum_{k=0}^{N-1} L^K + L^N \right) X_t. \end{aligned} \tag{2}$$

LX_t is the linear baseline extraction operator, HX_t is the intrinsic rotation component extraction operator, $HL^K X_t$ is the $k + 1$ rotation component, and $L^N X_t$ is the monotone trend component.

2.2. Principle of Permutation Entropy. Permutation entropy is sensitive to mutated signals, and it is an algorithm to describe the complexity of time series [23, 24]. The principle is as follows:

Given sequence $\{X(K), K = 1, 2, \ldots, N\}$, and the phase space reconstruction is performed:

$$Z = \begin{pmatrix} x(1) & x(1+\tau) & \cdots & x(1+(d-1)\tau) \\ x(2) & x(2+\tau) & \cdots & x(2+(d-1)\tau) \\ \vdots & \vdots & \vdots & \vdots \\ x(K) & x(K+\tau) & \cdots & x(K+(d-1)\tau) \end{pmatrix}. \quad (3)$$

d is the embedded dimension, τ is the delay time, and k is the reconstructed component.

Put the matrix Z each row in the sequence is arranged in ascending order:

$$x(t + R_1\tau) \le x(t + R_2\tau) \le \cdots \le x(t + R_d\tau). \quad (4)$$

t is the number of columns indexed, and $R_1, R_2, \ldots, R_d$ is the location of each element in the $X(K)$.

Define x_i^d as any set of reconstructed sequences, $0 \le R \le d!$. For the d-dimensional phase space mapping, there are the possibility of $d!$ arrangement and the possibility $P_1, P_2, \ldots, P_i$ of each sequence calculated. For the time series $X(K)$, there are i arrangement modes of H_p:

$$H_p(d) = -\sum P_i \ln(P_i). \quad (5)$$

When $P = m!$, $H_p(d)$ will reach the maximum value of $\ln(m!)$; in order to facilitate the comparison, the permutation entropy is often normalized:

$$H_p = \frac{H_p(d)}{\ln(m!)}. \quad (6)$$

The size of H_p represents the random degree of time series. The smaller H_p is, the more regular the corresponding time series is, and vice versa.

It should be noted that when the permutation entropy algorithm is carried out, the time delay τ has little effect on the time series, while the insertion dimension d is too small or too large, which will affect the construction accuracy of the reconstruction matrix. Bandt [30, 31] suggested that the dimension should be selected from 3 to 7; the results of the sample entropy obtained by calculation are highly reasonable in statistical theory. Therefore, the insertion dimension $d = 5$, and the time delay $\tau = 1$.

2.3. Principle of Singular Value Decomposition. As a nonlinear filtering method, SVD decomposes the matrix containing signal information into a series of singular values and time-frequency subspaces corresponding to singular value vectors from the perspective of matrix, which can eliminate noise to the maximum extent and retain useful information with fault signals, and has been widely used in the field of signal analysis [27, 28].

Suppose there is a signal to be decomposed $Y = (y(1), y(2), \ldots, y(n))$; an $m \times n$-order Hankel matrix is constructed for this signal:

$$H = \begin{bmatrix} y(1) & y(2) & \cdots & y(n) \\ y(2) & y(3) & \cdots & y(n+1) \\ \vdots & \vdots & \vdots & \vdots \\ y(N-n+1) & y(N-n+2) & \cdots & y(N) \end{bmatrix}. \quad (7)$$

N is the length of the signal to be decomposed, $1 < n < N$; $m = N - n + 1$; $H \in R^{m*n}$.

SVD decomposes the resulting matrix as follows:

$$H = USV^T. \quad (8)$$

$$S = \begin{cases} \left(\operatorname{diag}\left(\sigma_1, \sigma_2, \ldots, \sigma_q\right), 0\right), & m \le n, \\ \left(\operatorname{diag}\left(\sigma_1, \sigma_2, \ldots, \sigma_q\right), 0\right)^T, & m > n. \end{cases} \quad (9)$$

$U = (u_1, u_2, \ldots, u_m) \in R^{m*n}$ and $V = (v_1, v_2, \ldots, v_n) \in R^{m*n}$ are two orthogonal matrices; $S \in R^{m*n}$, determined by the relationship between m and n, 0 stands for zero matrix, $q = \min(m, n)$, and then the singular value of matrix H is $\sigma_1 \ge \sigma_2 \ge \cdots \ge \delta_q \ge 0$, $\sigma_i = (i = 1, 2, \ldots, q)$.

It should be noted that when creating a signal through the Hankel matrix, the number of rows m and columns n can be determined according to the following principles [27, 28]; when the signal length N is even, take $m = (N + 1)/2$, $n = N/2$; q takes the maximum value $q = N/2$. When the signal length N is odd, take $m = (N + 1)/2$, $n = (N + 1)/2$; q takes the maximum value $q = (N + 1)/2$.

The sequence formed by the singular value of the descending order is set as $\delta_i = (i = 0, 1, 2, \ldots, q)$; then the former singular values are subtracted from the latter singular values; that is, $b_i = \delta_i - \delta_{i+1} = 0, 1, 2, \ldots, q - 1$; then, the new sequence composed of b_i is the singular value difference spectrum. It can automatically select the effective order according to the difference of contribution of useful signal and noise signal to singular value energy. If the maximum mutation occurs at the position of the S point, the noise reduction can be realized when the reconstruction order is selected before the S point [28, 29].

2.4. Steps of the Signal Noise Reduction Method for ITD-PE-SVD

(1) Firstly, carry out ITD decomposition on collected vibration signals to obtain a series of PRC components

(2) According to formulas (4)–(6), calculate the arrangement entropy of PRC components

(3) According to the results of many simulation experiments and the principle of permutation entropy calculation, the threshold value of permutation entropy is set to 2, and the appropriate PRC component is selected for reconstruction, so as to achieve a noise reduction effect

(4) Perform SVD decomposition on the reconstructed signal again according to formula (8), and select suitable singular values to reconstruct the characteristic signal again according to the decomposed singular value differential spectrogram, so as to

achieve the secondary noise reduction effect and obtain the final denoised signal

(5) Analyze the characteristic frequency of the final denoised signal to judge the fault reason of the unit

The technical route is shown in Figure 1.

3. Simulation Signal and Analysis

In order to preliminarily judge the rationality of this method, the simulation signal is constructed according to the frequency characteristics of the hydraulic turbine under actual operating conditions.

Assuming that the unit frequency is 2 Hz and the sampling frequency is 500 Hz, the simulation signal without noise x1 contains four characteristic frequencies, namely, 1 Hz, 2 Hz, 4 Hz, and 7.5 Hz. The simulated noiseless waveform and spectrum diagram are shown in Figure 2. Consider adding a random white Gaussian noise $x2$ and a pulse signal $x3$; the signal after noise addition is x, and the waveform and spectrum after noise addition are shown in Figure 3. The formula for setting the simulation waveform is shown in the following:

$$\begin{aligned} x1 &= 6\sin(4\pi t) + 1.5\sin(15\pi t) + 4.5\sin(8\pi t) + 1.8\sin(2\pi t),\\ x2 &= 20\mathrm{rand}n(1{:}\ 5000),\\ x3 &= 35 * \mathrm{pulstran}(T, D, \text{'tripuls'}, 0.0000001, 0),\\ x &= x1 + x2 + x3. \end{aligned} \tag{10}$$

T is the time axis, generally a one-dimensional array, and D is the sampling interval.

It can be seen from the figures that when the simulated signal contains noise and abnormal pulse, the waveform is abnormally disorderly, and there are many interference frequencies in the spectrum diagram. Because of the existence of interference frequencies, the fault features are difficult to extract in the spectrum diagram, which may lead to misjudgment of the actual unit fault.

The proposed ITD-PE-SVD denoising method is used to process the noised signal. At the same time, in order to verify the effectiveness and superiority of the proposed method, the LMD-PE-SVD and EMD-PE-SVD are used to process the noised signal. The waveform and spectrum diagram of the three methods are shown in Figures 4–6.

It can be seen from Figures 4–6 that the simulated frequencies of 1 Hz, 2 Hz, 4 Hz, and 7.5 Hz are all extracted after being processed by four methods. However, after being processed by LMD-PE-SVD and EMD-PE-SVD, there are many interference frequencies around the signal, and the overall information is not fully reflected. After EMD-PE-SVD method, due to the presence of modal aliasing in the EMD decomposition process, the waveform is distorted.

After the ITD-PE-SVD denoising processing, not only the characteristic frequency can be clearly observed, but also the waveform diagram is almost completely close to Figure 2 (simulation without noise waveform and spectrum diagram), with smaller error, less surrounding interference, and better signal integrity, which fully demonstrates the effectiveness of the ITD-PE-SVD noise reduction method.

In order to quantitatively analyze the noise reduction performance, correlation coefficient (R) and signal-to-noise ratio (SNR) are taken as quantitative analysis indexes. The correlation coefficient refers to the correlation degree between the original signal and the denoised signal. The closer the value is to 1, the better the fitting degree between the denoised signal and the original signal is, and the more useful information of the original signal is retained [32–34]. The signal-to-noise ratio refers to the ratio of the original signal energy to the noise energy. The higher the signal-to-noise ratio, the better the denoising effect is [34–36]. The formula is as follows:

$$\begin{aligned} R &= \frac{\sum_{i=1}^{N} v_i \widehat{v}_i}{\sqrt{\sum_{i=1}^{N} v_i^2 \sum_{i=1}^{N} \widehat{v}_i^2}},\\ \mathrm{SNR} &= 10\lg \frac{\sum_{i=1}^{N} v_i^2}{\sum_{i=1}^{N} \left(v_i - \widehat{v}_i\right)^2}. \end{aligned} \tag{11}$$

N is the number of signal sampling points, v_i is the original signal, $\widehat{v}_i$ is the estimation of v_i, and lg is the logarithm based on 10.

The noise reduction performance indexes of each method are shown in Table 1. It can be seen that after ITD-PE-SVD denoising method is used to process the data containing noise and pulse, the data correlation is as high as 0.9956 and the signal-to-noise ratio is larger, and the comprehensive performance index is better than LMD-PE-SVD and EMD-PE-SVD, which shows the effectiveness of this method. At the same time, it also shows that the method maximizes the elimination of noise and retains useful information with fault signals and has a good effect on the data containing noise and pulse.

4. Engineering Examples

In order to verify the feasibility and effectiveness of this method in practical engineering application, the X-direction and Y-direction swing vibration data at the rated output of a hydropower station in China are selected to collect. The turbine model is HL220-LJ-410, the unit speed is 136r/min, and the acquisition frequency is 500 Hz. Some continuous data are selected and processed by ITD-PE-SVD.

The waveform and spectrum are shown in Figures 7–10. Among them, Figures 7 and 8 are the upper guide X-direction swing data waveform, spectrum diagram, and the upper guide X-direction swing waveform and spectrum diagram after the ITD-PE-SVD noise reduction. Figures 9 and 10 are the upper guide Y-direction swing data waveform, spectrum diagram, and the upper guide Y-direction swing waveform and spectrum diagram after the ITD-PE-SVD noise reduction.

It can be seen from the figures that the swing signal of the unit contains a large amount of background noise, and the noise distribution is uneven. After the denoising processing

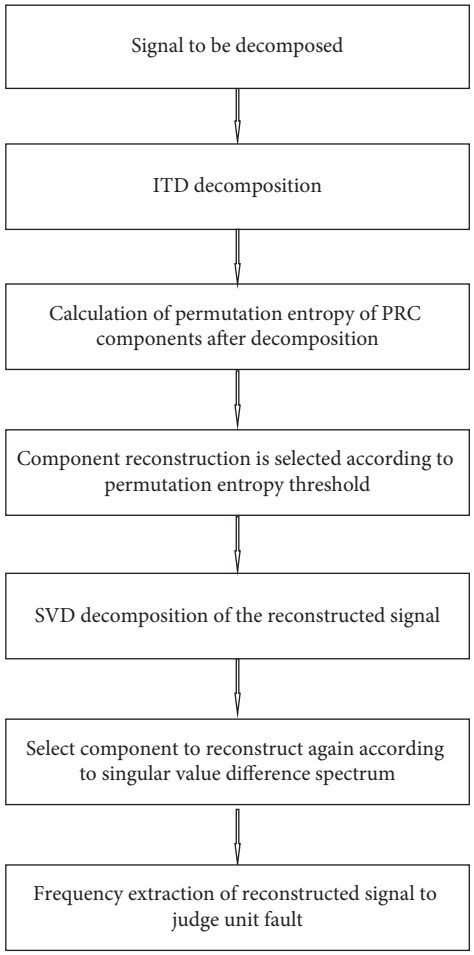

Figure 1: Denoising flowchart.

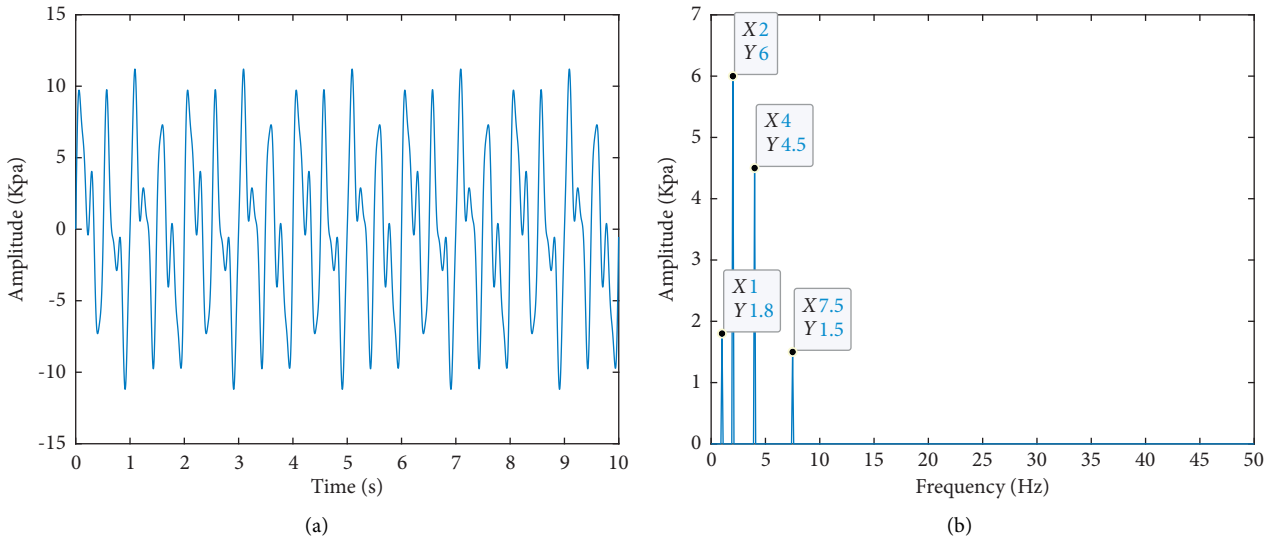

Figure 2: Simulation without noise waveform and spectrum diagram. (a) Waveform diagram. (b) Spectrogram.

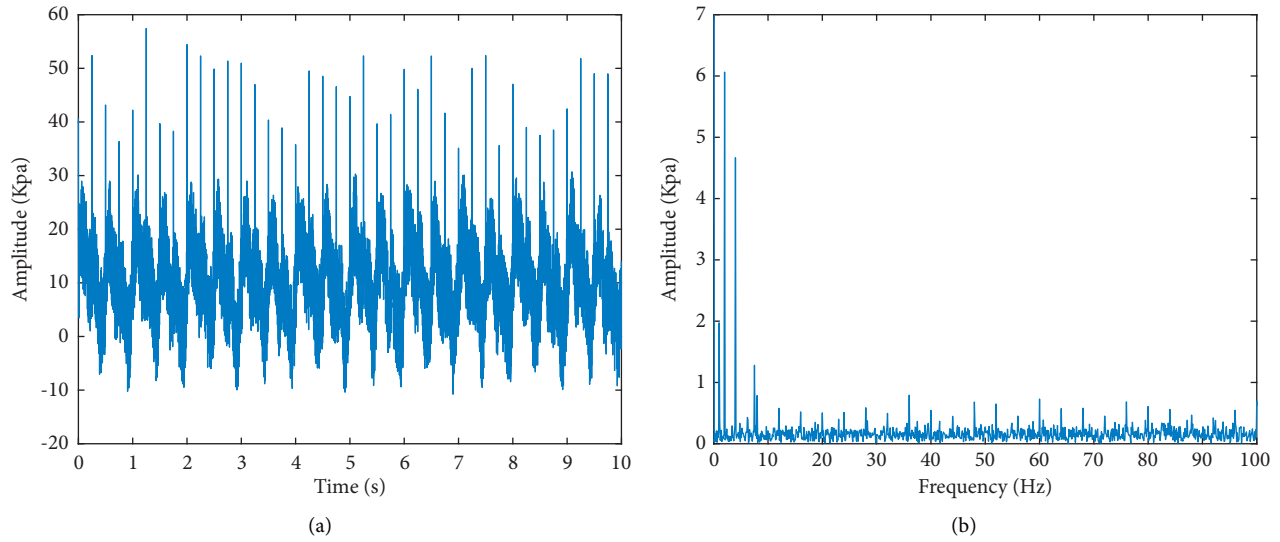

Figure 3: Simulation of noise addition waveform and spectrum diagram. (a) Waveform diagram. (b) Spectrogram.

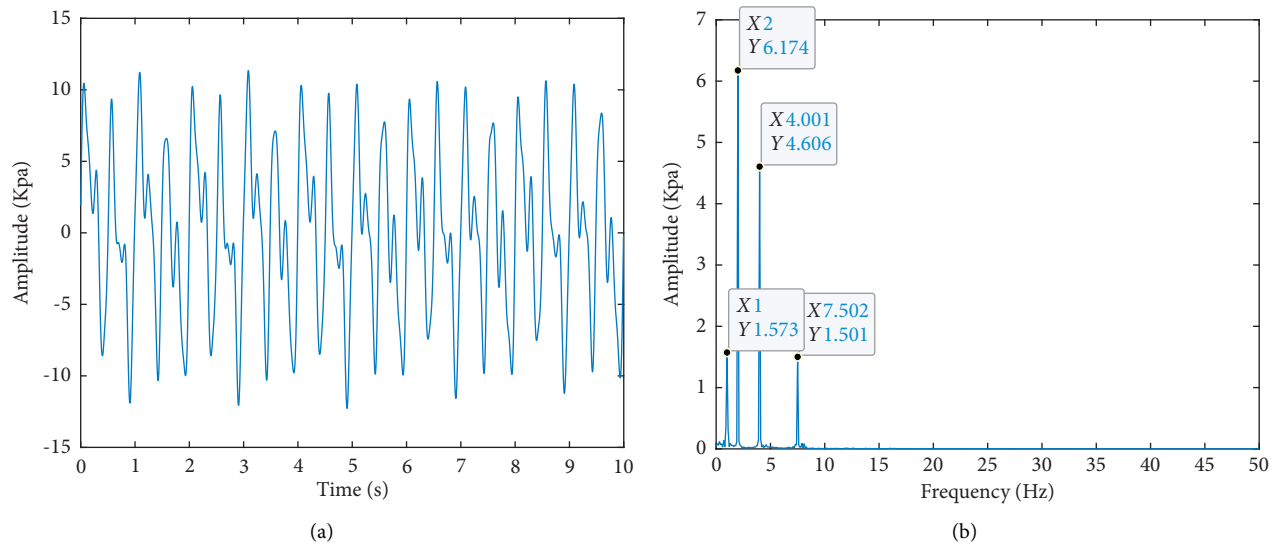

Figure 4: (a) Waveform diagram and (b) spectrogram after LMD-PE-SVD noise reduction.

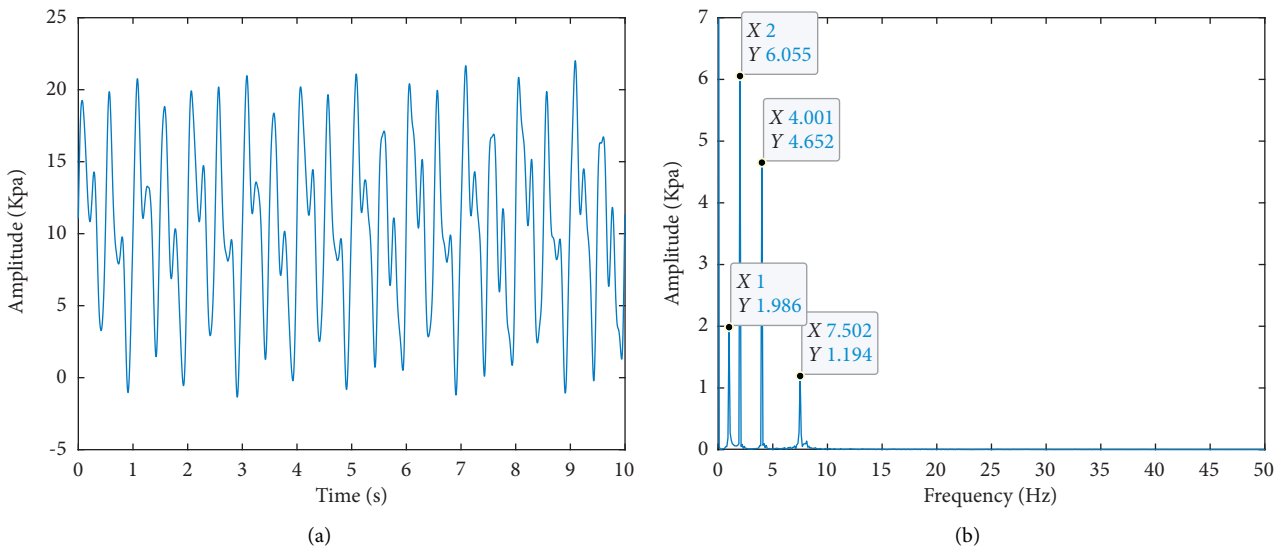

Figure 5: (a) Waveform diagram and (b) spectrogram after EMD-PE-SVD noise reduction.

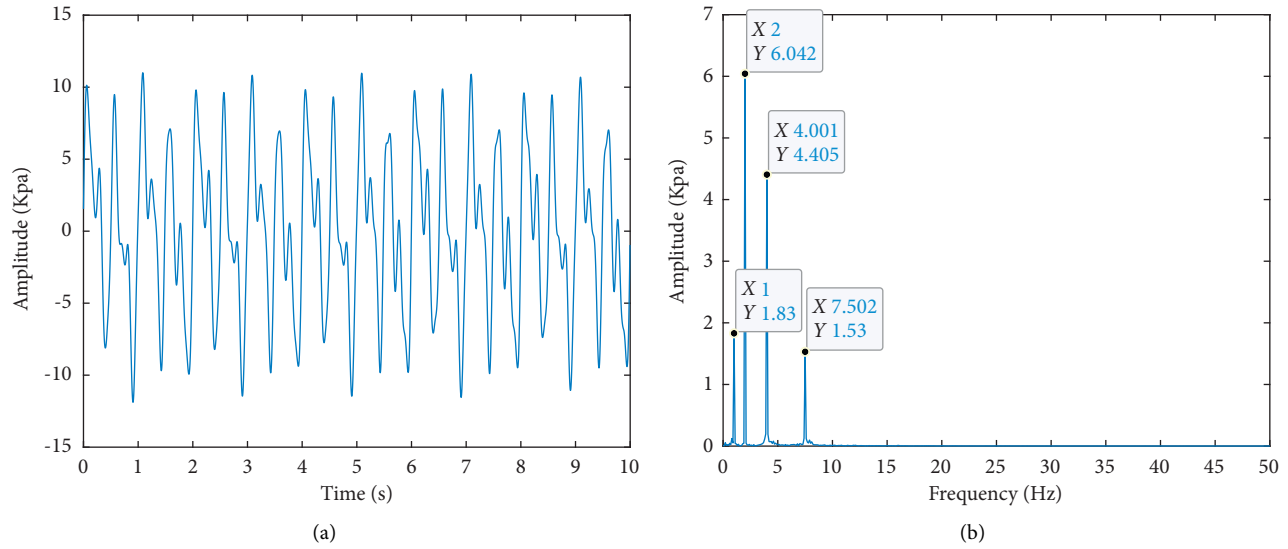

Figure 6: (a) Waveform diagram and (b) spectrogram after ITD-PE-SVD noise reduction.

Table 1: Related index values.

	Correlation coefficient	Signal-to-noise ratio
LMD-PE-SVD	0.9906	17.2549
EMD-PE-SVD	0.9910	18.2341
ITD-PE-SVD	0.9956	20.5502

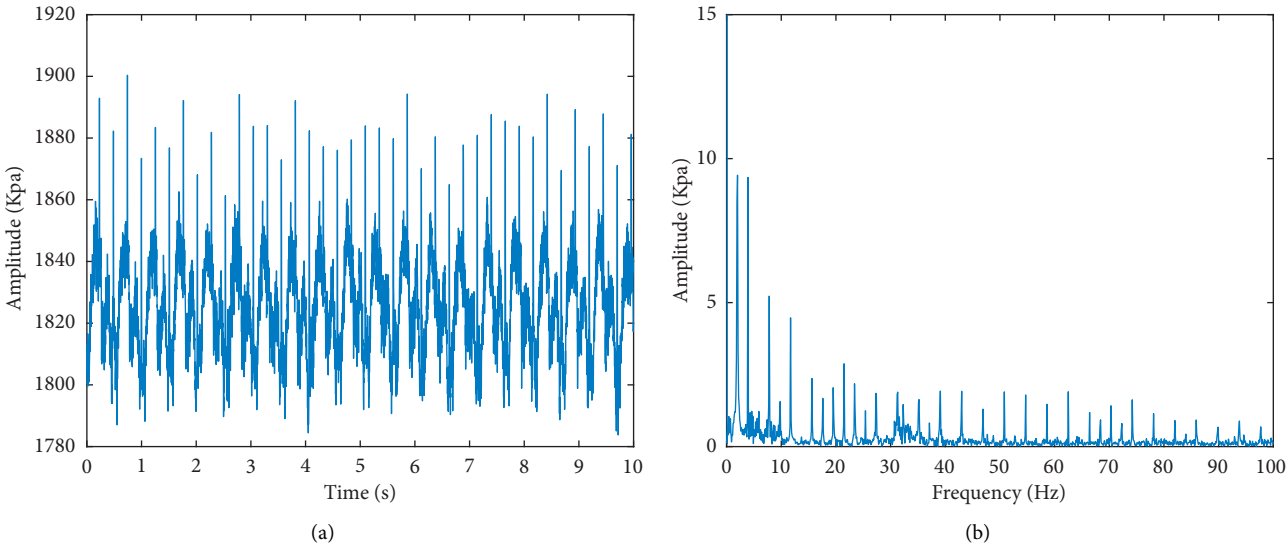

Figure 7: (a) Waveform diagram and (b) spectrogram of the upper guide X-direction swing data.

of the ITD-PE-SVD method proposed in this paper, the background noise is well filtered, and the waveform diagram is very clear, which further verifies the effectiveness of the method in engineering.

According to the frequency spectrum analysis of the denoised data of the unit, the frequency characteristics are 1, 2, 4, and 6 times of the frequency conversion of the unit, and there is no influence of other interference frequencies. According to [37], it can be seen that the vibration amplitude of the unit exceeds the specified standard due to mechanical factors, and the reason may be caused by the asymmetry or mass imbalance of the unit.

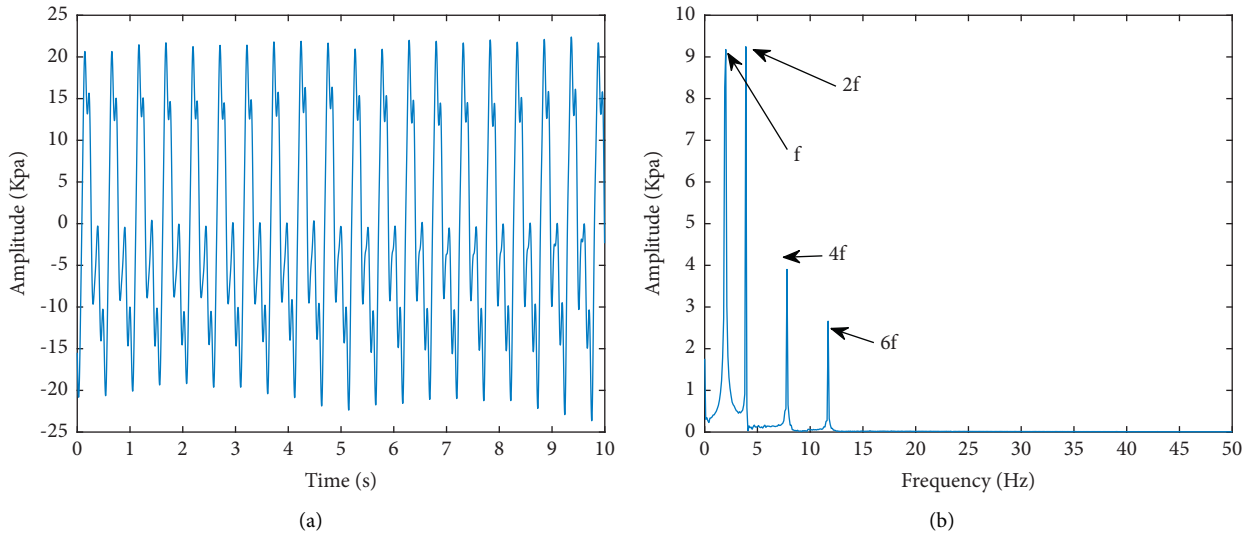

Figure 8: (a) Waveform diagram and (b) spectrogram of the upper guide *X*-direction swing data after ITD-PE-SVD noise reduction.

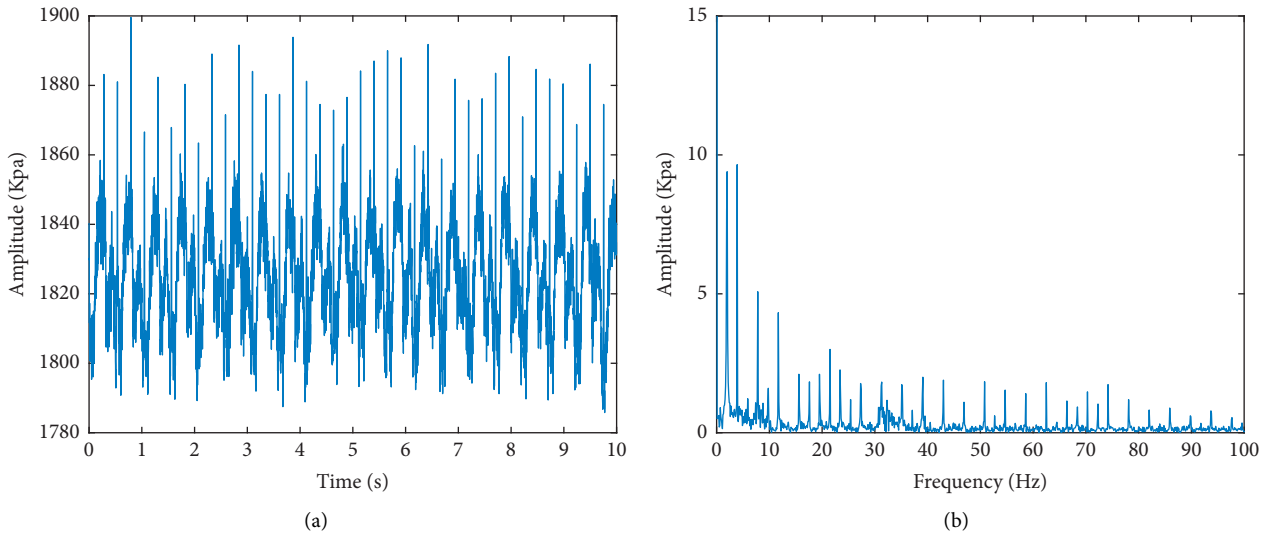

Figure 9: (a) Waveform diagram and (b) spectrogram of the upper guide *Y*-direction swing data.

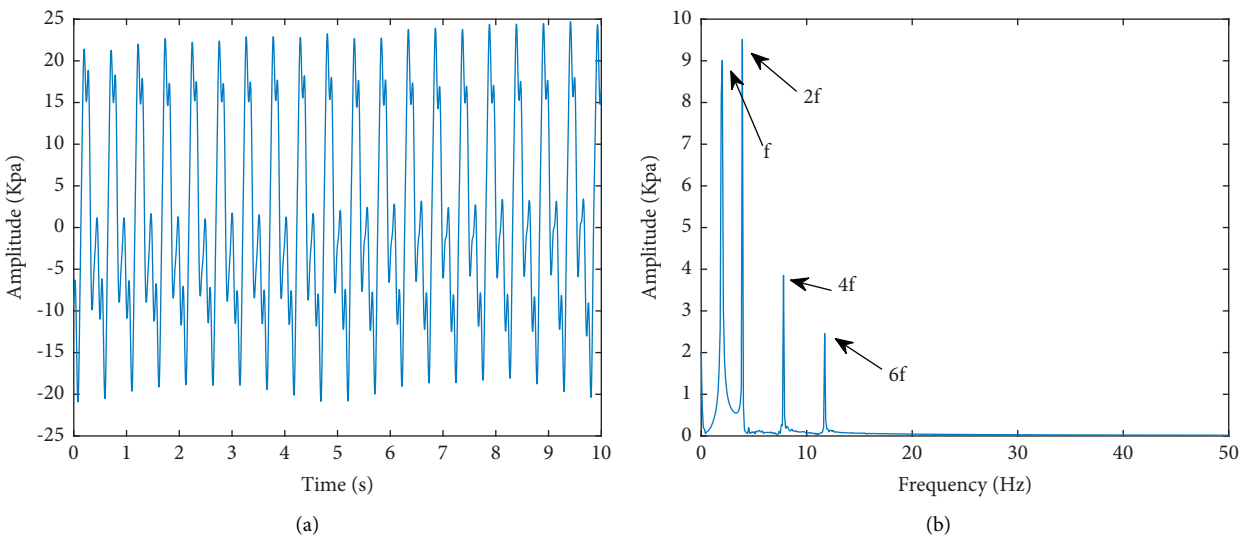

Figure 10: (a) Waveform diagram and (b) spectrogram of the upper guide *Y*-direction swing data after ITD-PE-SVD noise reduction.

5. Conclusion

In this paper, by combining the advantages of inherent time-scale decomposition, permutation entropy, and singular value decomposition, a denoising method based on ITD-PE-SVD is proposed to solve the problem that it is difficult to extract the vibration signal features of hydrogenerator unit under the background of strong background noise and complex electromagnetic interference.

(1) The ITD-PE-SVD denoising method is compared with LMD-PE-SVD and EMD-PE-SVD denoising methods through simulation experiments. At the same time, the correlation coefficient and signal-to-noise ratio are taken as quantitative indicators to analyze the noise reduction performance. It is found that after signal noise reduction processing by this method, data with correlation coefficient as high as 0.9956 and larger signal-to-noise ratio can be obtained, which can eliminate noise to the maximum extent while retaining useful information with fault signals. It has good noise reduction and pulse effect and avoids the modal aliasing in the EMD decomposition process.

(2) Through the analysis of the measured X- and Y-direction swing data of the upper guide of the hydrogenerator unit, it is found that this method can effectively reduce the noise of the measured unit data and accurately extract the characteristic frequency of the vibration signal, so as to determine the vibration reason of the unit through the frequency.

(3) The ITD-PE-SVD denoising method proposed in this paper can effectively extract the vibration signal characteristics of hydrogenerator units under the background of strong background noise and complex electromagnetic interference and provide a theoretical basis for subsequent fault diagnosis. It is convenient scientific and reasonable formulation of condition-based maintenance plans, greatly reduces the diagnosis time of power plants for complex hydraulic faults in actual operation, and thus improves the power generation efficiency and promotes the safety and stability of units and power grids.

Data Availability

The data used to support the findings of this study are available from the corresponding author upon request.

Conflicts of Interest

The authors declare that they have no conflicts of interest.

Acknowledgments

The study was supported by the following fund projects: (1) Henan Province Key R & D and Promotion Project (Science and Technology Research) in 2021 (212102311054); (2) Training Program for Young Key Teachers in Colleges and Universities of Henan Province in 2019 (2019GGJS097); (3) Hunan Key Laboratory of Renewable Energy Power Technology (Changsha University of Technology) Open Fund Project (2016ZNDL001).

References

[1] H. Gao, L. Liang, X. Chen, and G. Xu, "Feature extraction and recognition for rolling element bearing fault utilizing short-time Fourier transform and non-negative matrix factorization," *Chinese Journal of Mechanical Engineering*, vol. 28, no. 1, pp. 96–105, 2014.

[2] J. Chen, Z. Li, J. Pan et al., "Wavelet transform based on inner product in fault diagnosis of rotating machinery: a review," *Mechanical Systems and Signal Processing*, vol. 70-71, pp. 1–35, 2016.

[3] S. J. Loutridis, "Damage detection in gear systems using empirical mode decomposition," *Engineering Structures*, vol. 26, no. 12, pp. 1833–1841, 2004.

[4] H. Darong, K. Lanyan, M. Bo, Z. Ling, and S. Guoxi, "A new incipient fault diagnosis method combining improved RLS and LMD algorithm for rolling bearings with strong background noise," *IEEE Access*, vol. 6, pp. 26001–26010, 2018.

[5] L. Li, H. Cai, H. Han, J. Qingtang, and Ji Hongbing, "Adaptive short-time Fourier transform and synchrosqueezing transform for non-stationary signal separation," *Signal Processing*, vol. 166, pp. 107231.1–107231.15, 2020.

[6] M. S. Santhoshi, K. Sharath Babu, S. Kumar, and D. Nandan, "An investigation on rolling element bearing fault and real-time spectrum analysis by using short-time fourier transform," in *Proceedings of the International Conference on Recent Trends in Machine Learning, IoT, Smart Cities and Applications*, Hyderabad, India, October 2021.

[7] L. I. Heng, Q. Zhang, X. Qin, and Y. Sun, "Fault diagnosis method for rolling bearings based on short-time Fourier transform and convolution neural network," *Journal of Vibration and Shock*, vol. 37, 2018.

[8] Z. P. Xu Zeng-pu, L. X. Hu Li-xiang, and Y. M. Qi Yu-ming, "Influence of window width selection in fault diagnosis of loudspeaker based on Short-time Fourier Transform," in *Proceedings of the IEEE International Conference on Computer Science & Information Technology*, Chengdu, China, July 2010.

[9] W. Deng, S. Zhang, H. Zhao, and X. Yang, "A novel fault diagnosis method based on integrating empirical wavelet transform and fuzzy entropy for motor bearing," *IEEE Access*, vol. 6, pp. 35042–35056, 2018.

[10] C. Mateo and J. A. Talavera, "Bridging the gap between the short-time Fourier transform (STFT), wavelets, the constant-Q transform and multi-resolution STFT," *Signal, Image and Video Processing*, vol. 14, no. 8, pp. 1535–1543, 2020.

[11] B. Yan and A. Miyamoto, "A comparative study of modal parameter identification based on wavelet and hilbert-huang transforms," *Computer-Aided Civil and Infrastructure Engineering*, vol. 21, no. 1, pp. 9–23, 2006.

[12] S. Selami, M. S. Mecibah, Y. Debbah, and T. E. Boukelia, "Gear crack detection using residual signal and empirical mode decomposition," *Mechanics and Mechanical Engineering*, vol. 22, no. 4, pp. 1133–1144, 2018.

[13] J. Zheng, M. Su, W. Ying, J. Tong, and Z. Pan, "Improved uniform phase empirical mode decomposition and its application in machinery fault diagnosis," *Measurement*, vol. 179, no. 2, Article ID 109425, 2021.

[14] X.-B. Wang, Z.-X. Yang, and X.-A. Yan, "Novel particle swarm optimization-based variational mode decomposition

method for the fault diagnosis of complex rotating machinery," *IEEE*, vol. 23, no. 1, pp. 68–79, 2018.

[15] M. Van, H. J. Kang, and K. S. Shin, "Rolling element bearing fault diagnosis based on non-local means de-noising and empirical mode decomposition," *IET Science, Measurement & Technology*, vol. 8, no. 6, pp. 571–578, 2014.

[16] Y. Yu, J. Cheng, and Z. Kang, "An ensemble local means decomposition method and its application to local rub-impact fault diagnosis of the rotor systems," *Measurement*, vol. 45, no. 3, pp. 561–570, 2012.

[17] S. Zhou, M. Xiao, P. Bartos, M. Filip, and G. Geng, "Remaining useful life prediction and fault diagnosis of rolling bearings based on short-time fourier transform and convolutional neural network," *Shock and Vibration*, vol. 2020, no. 4, 2020.

[18] T. Y. Wu and Y. L. Chung, "Misalignment diagnosis of rotating machinery through vibration analysis via the hybrid EEMD and EMD approach," *Smart Materials and Structures*, vol. 18, no. 9, Article ID 095004, 2009.

[19] J. Wu, P. Guo, Y. Cheng, H. Zhu, X.-B. Wang, and X. Shao, "Ensemble generalized multiclass support-vector-machine-based health evaluation of complex degradation systems," *IEEE*, vol. 25, no. 5, pp. 2230–2240, 2020.

[20] Z. Feng, X. Lin, and M. J. Zuo, "Joint amplitude and frequency demodulation analysis based on intrinsic time-scale decomposition for planetary gearbox fault diagnosis," *Mechanical Systems and Signal Processing*, vol. 72-73, pp. 223–240, 2016.

[21] M. G. Frei and I. Osorio, "Intrinsic time-scale decomposition: time-frequency-energy analysis and real-time filtering of non-stationary signals," *Proceedings of the Royal Society A: Mathematical, Physical & Engineering Sciences*, vol. 463, no. 2078, pp. 321–342, 2007.

[22] J. Zeng, G. Wang, F. Zhang, and J. Ye, "The de-noising algorithm based on intrinsic time-scale decomposition," *Advanced Materials Research*, vol. 422, pp. 347–352, 2012.

[23] X. An, D. Jiang, J. Chen, and C. Liu, "Application of the intrinsic time-scale decomposition method to fault diagnosis of wind turbine bearing," *Journal of Vibration and Control*, vol. 18, no. 2, pp. 240–245, 2012.

[24] C. Bandt and B. Pompe, "Permutation entropy: a natural complexity measure for time series," *Physical Review Letters*, vol. 88, no. 17, Article ID 174102, 2002.

[25] Z. Guo, M. Liu, Y. Wang, and H. Qin, "A new fault diagnosis classifier for rolling bearing united multi-scale permutation entropy optimize VMD and cuckoo search SVM," *IEEE Access*, vol. 8, no. 99, pp. 153610–153629, 2020.

[26] X. Xue, C. Li, S. Cao, J Sun, and L Liu, "Fault diagnosis of rolling element bearings with a two-step scheme based on permutation entropy and random forests," *Entropy*, vol. 21, no. 1, 2019.

[27] H. Jiang, J. Chen, G. Dong, T. Liu, and G. Chen, "Study on Hankel matrix-based SVD and its application in rolling element bearing fault diagnosis," *Mechanical Systems and Signal Processing*, vol. 52-53, pp. 338–359, 2015.

[28] R. Golafshan and K. Yuce Sanliturk, "SVD and Hankel matrix based de-noising approach for ball bearing fault detection and its assessment using artificial faults," *Mechanical Systems and Signal Processing*, vol. 70-71, pp. 36–50, 2016.

[29] J. Xu, S. Tong, F. Cong, and J. Chen, "Slip Hankel matrix series-based singular value decomposition and its application for fault feature extraction," *IET Science, Measurement & Technology*, vol. 11, no. 4, pp. 464–472, 2017.

[30] F. E. Pose, L. Bautista, F. Gianmuso, and F. O. Redelico, "On the permutation entropy bayesian estimation," *Communications in Nonlinear Science and Numerical Simulation*, vol. 99, Article ID 105779, 2021.

[31] S. Sharma, S. K. Tiwaria, and S. Singh, "Integrated approach based on flexible analytical wavelet transform and permutation entropy for fault detection in rotary machines," *Measurement*, vol. 169, Article ID 105779, 2021.

[32] J. Wu, P. Guo, Y. Cheng et al., "Ensemble generalized multiclass support-vector-machine-based health evaluation of complex degradation systems," *IEEE/ASME Transactions on Mechatronics*, vol. 25, no. 5, pp. 2230–2240, 2020.

[33] Y. Ren, P. Liu, L. Hu et al., "Research on noise reduction method of pressure pulsation signal of draft tube of hydropower unit based on ALIF-SVD," *Shock and Vibration*, vol. 2021, no. 1, 11 pages, 2021.

[34] X. An and J. Yang, "Denoising of hydropower unit vibration signal based on variational mode decomposition and approximate entropy," *Transactions of the Institute of Measurement and Control*, vol. 38, no. 3, 2016.

[35] D. Wang, X. Zhang, C. Yu, and Z. Tang, "Reversible data hiding by using adaptive pixel value prediction and adaptive embedding bin selection," *IEEE Signal Processing Letters*, vol. 26, no. 11, pp. 1713–1717, 2019.

[36] Z.-X. Yang, G. Yu, J. Zhao, P. K. Wong, and X.-B. Wang, "Online equivalent degradation indicator calculation for remaining charging-discharging cycle determination of lithium-ion batteries," *IEEE Transactions on Vehicular Technology*, vol. 70, no. 7, pp. 6613–6625, 2021.

[37] S. Dong, C. F. Tao, and C. Si, "Diagnosis and identification of vibration accident for hydrogenerator unit," *Journal of Hydrodynamics*, vol. 15, no. 1, 2000.